












Black hole virial masses from single-epoch photometry: the miniJPAS test case

Jonás Chaves-Montero¹★, Silvia Bonoli^{1,2}, Benny Trakhtenbrot³, Alejandro Fernández-Centeno⁴, Carolina Queiroz^{5,6}, Luis A. Díaz-García⁷, Rosa María González Delgado⁷, Antonio Hernán-Caballero⁸, Carlos Hernández-Monteagudo^{9,10}, Carlos López-Sanjuan¹¹, Roderik Overzier^{12,13}, David Sobral¹⁴, L. Raul Abramo⁶, Jailson Alcaniz^{5,12}, Narciso Benitez⁷, Saulo Carneiro¹⁵, A. Javier Cenarro¹¹, David Cristóbal-Hornillos⁸, Renato A. Dupke^{12,16,17}, Antonio Marín-Franch¹¹, Claudia Mendes de Oliveira¹³, Mariano Moles^{7,8}, Laerte Sodré Jr.¹³, Keith Taylor¹⁸, Jesús Varela¹¹, Héctor Vázquez Ramió¹¹, and Tamara Civera⁸.

(Affiliations are listed after the references)

ABSTRACT

Precise measurements of black hole (BH) masses are essential to understanding the coevolution of these sources and their host galaxies. In this work, we develop a novel approach to compute BH virial masses using measurements of continuum luminosities and emission line widths from partially-overlapping, narrow-band observations of quasars; we refer to this technique as single-epoch photometry. This novel method relies on forward-modelling quasar observations to estimate the previous properties, which enables accurate measurements of emission line widths even for lines poorly resolved by narrow-band data. We assess the performance of this technique using quasars from the Sloan Digital Sky Survey (SDSS) observed by the miniJPAS survey, a proof-of-concept project of the J-PAS collaboration covering $\simeq 1 \text{ deg}^2$ of the northern sky using the 56 J-PAS narrow-band filters. We find remarkable agreement between BH masses from single-epoch SDSS spectra and single-epoch miniJPAS photometry, with no systematic difference between these and a scatter ranging from 0.4 to 0.07 dex for masses from $\log(M_{\text{BH}}/M_{\odot}) \simeq 8$ to 9.75, respectively. Reverberation mapping studies show that single-epoch masses approximately present 0.4 dex precision, letting us conclude that our novel technique delivers BH masses with only mildly worse precision than single-epoch spectroscopy. The J-PAS survey will soon start observing thousands of square degrees without any source preselection other than the photometric depth in the detection band, and thus single-epoch photometry has the potential to provide details on the physical properties of quasar populations not satisfying the preselection criteria of previous spectroscopic surveys.

Key words: quasars: supermassive black holes – quasars: emission lines – galaxies: photometry – galaxies: active – line: profiles

1 INTRODUCTION

Quasars are the most luminous persistent sources known, enabling us to study the Universe from late to very early epochs (e.g., Fan et al. 2006; Bañados et al. 2018; Yang et al. 2020a; Wang et al. 2021). For example, quasars are excellent large-scale structure tracers at redshifts where the number density of bright galaxies is too low for statistical studies (e.g., Busca et al. 2013; Castorina et al. 2019; Hou et al. 2021), provide crucial information about the reionization history of the Universe (e.g., Bañados et al. 2018; Davies et al. 2018; Wang et al. 2020; Yang et al. 2020b), and have been proposed as

standardisable candles (e.g., Watson et al. 2011; Wang et al. 2014; Risaliti & Lusso 2019), which provides a new avenue to extend Hubble parameter constraints towards high redshift.

The accepted physical picture is that a quasar is powered by the accretion of matter onto a supermassive black hole (SMBH, e.g., Hoyle & Fowler 1963; Salpeter 1964; Lynden-Bell 1969), which is inferred to exist at the centre of every massive galaxy (e.g., Kormendy & Richstone 1995; Magorrian et al. 1998; Ferrarese & Merritt 2000). The discovery of correlations between multiple galaxy properties and SMBH mass (e.g., Magorrian et al. 1998; Ferrarese & Merritt 2000; Gebhardt et al. 2000; Gültekin et al. 2009; Kormendy & Ho 2013; McConnell & Ma 2013) suggests coevolution between SMBHs and their host galaxies, during which the energy released

★ E-mail: jonas.chaves@dipc.org

by the accreting SMBH self-regulates its growth and impacts the evolution of its host (Silk & Rees 1998; King 2003; Di Matteo et al. 2005). The coevolution scenario is also supported by the similar redshift evolution of the cosmic SMBH accretion rate and the cosmic star formation rate up to $z = 4$ (Merloni et al. 2004; Silverman et al. 2008; Shankar et al. 2009; Aird et al. 2010; Delvecchio et al. 2014; Yang et al. 2018), and the need for active galactic nuclei feedback to explain the stellar-to-halo mass relation for massive galaxies in hydrodynamical simulations and semi-analytic models (e.g., Croton et al. 2006; Somerville et al. 2008; Dubois et al. 2012; Sijacki et al. 2015; Schaye et al. 2015; Weinberger et al. 2017; Pillepich et al. 2018). However, the nature of the SMBH-galaxy relation is still not completely understood; for instance, the presence of SMBHs with masses larger than $10^9 M_\odot$ at $z > 6$ poses an important question about the origin and fast growth of these objects (see Inayoshi et al. 2020, for a recent review).

In the local universe, SMBH masses are estimated by resolving the dynamics of stars (e.g., Davies et al. 2006; Onken et al. 2007) or gas (e.g., Hicks & Malkan 2008) within the SMBH’s gravitational sphere of influence. At cosmological distances, spatially resolving this region is impossible, and the standard approach to estimating SMBH masses for distant galaxies relies on measurements of the virial motion of gas in the broad-line region (BLR; e.g., Czerny & Hryniewicz 2011). The most precise method to compute virial masses is reverberation mapping (RM, e.g., Blandford & McKee 1982; Peterson 1993; Netzer & Peterson 1997), which yields robust SMBH mass estimates consistent with dynamical masses (e.g., Bentz et al. 2013). RM measures the velocity of clouds in the BLR from the width of broad emission lines and the BLR size from the time lag between continuum and emission line variability; to do so, it requires multiple spectroscopic observations over an extended time at high cadence (e.g., MacLeod et al. 2010; Bentz et al. 2013), which has limited the application of this technique to a few hundreds of sources so far (Kaspi et al. 2021).

The only method to estimate SMBH virial masses for a large number of sources is single-epoch spectroscopy (SES, e.g., Wandel et al. 1999; McLure & Jarvis 2002; Vestergaard 2002), which relies on the tight correlation between quasar continuum luminosity and BLR size (e.g., Kaspi et al. 2000, 2005; Bentz et al. 2006, 2009, 2013; Lira et al. 2018) to compute SMBH masses from a single spectrum. These lesser requirements translate into noisier SMBH mass estimates than RM, which require empirical calibration either from RM (e.g., Kaspi et al. 2000, 2005; Bentz et al. 2013) or internally based on the availability of multiple emission lines for the same object (e.g., McLure & Jarvis 2002; Vestergaard & Peterson 2006; Shen et al. 2011). Taken together with systematics involved in the measurement of line widths, these sources of uncertainty result in differences between SMBH masses from SES and RM as large as 0.5 dex (e.g., McLure & Jarvis 2002; Vestergaard & Peterson 2006; Shen 2013; Peterson 2014).

Traditionally, measuring SMBH masses was a prerogative of spectroscopic surveys because the spectral resolution of photometric surveys was too coarse to resolve even the broadest quasar emission lines, which present widths of thousands of km/s. In addition, photometric redshifts from broad-band photometry do not present enough precision for unambiguous line identification. The emergence of medium- and narrow-band photometric surveys continuously covering a large wavelength range such as the Subaru COSMOS 20 survey (Taniguchi et al. 2015; Sobral et al. 2018), the Advance Large Homogeneous Area Medium Band Redshift Astronomical survey (ALHAMBRA; Moles et al. 2008), the NEWFIRM Medium-Band Survey (NMBS; van Dokkum et al. 2009), the Survey for High- z Ab-

sorption Red and Dead Sources (SHARDS; Pérez-González et al. 2013), the Physics of the Accelerating Universe Survey (PAUS; Eriksen et al. 2019), and the Javalambre-Physics of the Accelerating Universe Astrophysical Survey (J-PAS; Benítez et al. 2014) are progressively changing this picture, as multi-band photometric surveys first reached enough spectral resolution to detect broad emission lines (Chaves-Montero et al. 2017; Lumberras-Calle et al. 2019), and then to detect narrow lines and resolve the profile of broad lines approximately (Alarcon et al. 2021; Bonoli et al. 2021b; Martínez-Solaeche et al. 2021).

In this work, we develop the first method to measure SMBH virial masses from narrow-band “photospectra”, i.e. photometric observations from a contiguous set of partially overlapping narrow-band filters. This technique estimates the virial velocity of BLR clouds from the width of broad emission lines and the size of the BLR from the continuum luminosity; given the similarity of this technique with single-epoch spectroscopy, we dub this approach as single-epoch photometry (SEP). We show that the resolution of J-PAS photospectra is too coarse for backward-modelling¹ emission line widths in an unbiased fashion; motivated by this, we combine forward-modelling quasar observations and Bayesian inference to measure continuum luminosities and emission line widths. To validate our methodology, we use 54 Sloan Digital Sky Survey (SDSS; York et al. 2000) quasars observed by the miniJPAS survey (Bonoli et al. 2021b), a proof-of-concept project of the J-PAS collaboration. By comparing SES masses from SDSS and SEP masses from miniJPAS, we find that single-epoch photometry delivers unbiased SMBH mass estimates with only slightly less precision than single-epoch spectroscopy measurements for most masses. Our findings open the possibility to study the physical properties of quasar populations not satisfying the preselection criteria of previous spectroscopic surveys that future narrow-band surveys like J-PAS will observe.

The paper is organised as follows. In §2, we introduce the dataset that we use to calibrate the performance single-epoch photometry. In §3, we describe our approach to measuring continuum luminosities, emission line properties, and SMBH virial masses from narrow-band data, and in §4 we use SDSS quasars observed by the miniJPAS survey to estimate the precision of the previous measurements. In §5, we summarise our main findings and conclude.

Throughout this paper we consider *Planck* 2015 cosmological parameters (Planck Collaboration et al. 2014): $\Omega_m = 0.314$, $\Omega_\Lambda = 0.686$, $\Omega_b = 0.049$, $\sigma_8 = 0.83$, $h = 0.67$, and $n_s = 0.96$. We use the term quasar to refer to unobscured active galactic nuclei with at least one emission line broader than 1000 km s^{-1} . Emission lines with central wavelength smaller and larger than $\lambda = 2000 \text{ \AA}$ are provided in vacuum and air wavelengths, respectively. All magnitudes are reported in the AB system (Oke & Gunn 1983). We use the symbol log to indicate decimal logarithms.

2 DATA

2.1 Narrow-band data: miniJPAS

The miniJPAS survey (Bonoli et al. 2021b) observed $\approx 1 \text{ deg}^2$ of the northern sky using the J-PAS filter system, which includes 54

¹ Backward-modelling refers to the process of measuring some target property directly from observations, while forward-modelling indicates the process of first producing plausible values of such property using a theoretical model, and then measuring it by comparing these values with observations.

partially-overlapping narrow-band filters of full width at half maximum FWHM $\approx 145 \text{ \AA}$ covering the optical range from 3780 to 9100 \AA and 2 broader filters expanding over the UV and the near-infrared up to approximately 3100 and 10 000 \AA , respectively. The observations were carried out using an interim camera mounted on the 2.5 m diameter Javalambre Survey Telescope at the Astrophysical Observatory of Javalambre, which will be the same telescope conducting observations for the J-PAS survey. This survey was designed to serve as a proof-of-concept for the J-PAS project (Benítez et al. 2014).

The footprint of miniJPAS covers the Extended Groth Strip (EGS) field partially, where ancillary data from the AEGIS (Davis et al. 2007) and SDSS (York et al. 2000) surveys are publicly available. To facilitate the comparison with other surveys, each pointing of miniJPAS was observed not only with all J-PAS filters, but also with the broad-band filters u , g , r , and i . The depth of miniJPAS in a circular aperture of $3''$ diameter reaches $m \approx 22 - 23.5$ AB at 5σ for the 54 narrow-band filters and up to $m = 24$ AB for the broader filters. The primary catalogue of this survey contains more than 64 000 sources detected in the r band with matched forced photometry in all other bands (see Bonoli et al. 2021b, for more details).

The J-PAS filter system² (Brauneck et al. 2018a,b) was designed to provide accurate photometric redshifts for both blue and red galaxies up to $z \sim 1$ (Benítez et al. 2009; Benítez et al. 2014), and for quasars up to $z \approx 6$ (Abramo et al. 2012; Chaves-Montero et al. 2017). The first results from miniJPAS confirmed the expectations of sub-percent photo- z precision (Bonoli et al. 2021b; Hernán-Caballero et al. 2021), the potential of the J-PAS filter system to detect and characterise emission line sources (Bonoli et al. 2021b; González Delgado et al. 2021; Martínez-Solaesche et al. 2021), and more specifically to capture the main features of low redshift quasars (Bonoli et al. 2021a) using QSFIT (Calderone et al. 2017). Furthermore, the WEAVE-QSO survey (Pieri et al. 2016) will follow-up with high spectral resolution $\sim 400k$ J-PAS quasars at $z > 2$, allowing to further test and calibrate our approach.

2.2 Spectroscopic data: SDSS

The SDSS survey (York et al. 2000) also observed the EGS field, and thus we can use quasars with single-epoch spectroscopy measurements from SDSS to estimate the performance of single-epoch photometry for miniJPAS. In this section, we describe the main characteristics of the SDSS data we use.

To validate our methodology, we use publicly available SES measurements from the 14th data release of the SDSS quasar value-added catalogue (SDSS14Q; Rakshit et al. 2020), which contains 526 356 sources observed by any of the stages of the SDSS survey up to and including this data release (York et al. 2000; Eisenstein et al. 2011; Dawson et al. 2013; Dawson et al. 2016). Quasars included in this catalogue satisfy two selection criteria: i -band absolute magnitude brighter than $M_i(z=2) = -20.5$ and at least one emission line broader than $\text{FWHM} = 500 \text{ km s}^{-1}$. For each source, the SDSS14Q catalogue includes the most robust spectroscopic redshift solution from SDSS (see Pâris et al. 2018), the FWHM and equivalent width (EW) of the broadest emission lines, the monochromatic continuum luminosity nearby these lines, and SMBH virial mass estimates

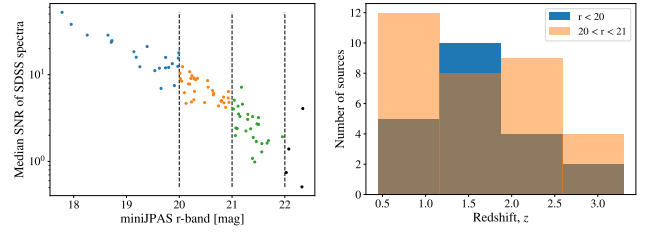


Figure 1. Properties of SDSS quasars with successful SES measurements observed by miniJPAS. Blue, orange, and green colours indicate the results for sources with $r < 20$, $20 < r < 21$, and $21 < r < 22$, respectively. The left panel shows the median SNR of SDSS spectra as a function of miniJPAS r -band magnitude, while the right panel displays the redshift distribution of quasars brighter than $r = 21$.

based on these key spectroscopic measurements. The spectral information was measured using the publicly available multi-component spectral fitting code PYQSOFIT³ (Guo et al. 2018), which uses multiple components to model the continuum emission and emission lines of each quasar separately (for a detailed description of the code and its applications see Guo et al. 2019; Shen et al. 2019).

2.3 Validation sample

We generate the quasar validation sample by cross-matching miniJPAS observations and the 12th data release of the SDSS quasar superset catalogue (SDSS12Q, Pâris et al. 2017), which contains visually inspected spectra and redshifts from any of the stages of the SDSS survey up to and including this data release. We find that miniJPAS observed 117 SDSS quasars and that 85 out of these present successful SES measurements from the SDSS14Q catalogue.

We generate a photospectrum for each source by combining $3''$ aperture magnitudes from each of the miniJPAS narrow-band filters. We use this type of magnitude due to the point-like nature of quasars, and we correct aperture to total magnitudes following a two-step procedure. First, we compute the median difference between $3''$ aperture magnitudes of bright, unsaturated stars from each miniJPAS tile and point spread function magnitudes from the Panoramic Survey Telescope and Rapid Response System 1 (Pan-STARRS1, Chambers et al. 2016). We use these offsets to correct the magnitudes of each tile separately, and then we compute the median difference between the resulting magnitudes and synthetic magnitudes obtained by convolving the spectra of 115 stars from the SDSS12Q catalogue with the J-PAS filter system. Finally, we apply these differences to the partially-corrected magnitudes. Note that this two-step approach corrects for both the finite size of $3''$ apertures and spectral offsets. For more details about this process, see Queiroz et al. (in prep.).

The miniJPAS survey conducted observations of most filters between May and October of 2018, and of a few filters in July 2019 (Bonoli et al. 2021b). Due to the variable nature of quasars, we could expect variability to manifest as artificial emission/absorption lines in miniJPAS photospectra due to filters observed at different epochs. The impact of variability is increasingly weaker for more luminous quasars (e.g., Hook et al. 1994; MacLeod et al. 2012; Meusinger & Weiss 2013; Kozłowski et al. 2016; Caplar et al. 2017), and the expected level of optical variability is ~ 0.1 AB per 100 rest-frame

² <http://svo2.cab.inta-csic.es/svo/theory/fps3/index.php?mode=browse&name=0AJ&asttype=>

³ <https://github.com/legolason/PYQSOFIT/>

days for the faintest sources. The maximum time span between miniJPAS observations is approximately 400 days, so we expect the largest band-to-band magnitude fluctuations to be smaller than 0.2 and 0.1 AB for quasars at $z = 1$ and 3, respectively. Taken together with the high luminosity of miniJPAS quasars (see §4.1), we expect minimal impact of variability on miniJPAS observations. On the other hand, the difference between SDSS and miniJPAS observations is of the order of years for some sources, and thus we expect variability to affect the comparison between single-epoch spectroscopy and photometry measurements. Note that the virial theorem suggests that a change of X dex in continuum luminosity manifests as a $-0.25 X$ dex difference in FWHM.

In the left panel of Fig. 1, we display the median spectral signal-to-noise ratio (SNR) of the 85 SDSS quasars with successful SES measurements as a function of their miniJPAS r -band magnitude. Blue, orange, and green dots indicate the results for sources with $r < 20$, $20 < r < 21$, and $21 < r < 22$, respectively. As we can see, most sources with r -band magnitude fainter than $r = 21$ present an SDSS spectrum with median SNR smaller than 4. Multiple authors have investigated the impact of SNR on the robustness of SES measurements (e.g., Shen et al. 2011; Denney et al. 2016; Shen et al. 2019), finding that the precision of SES masses decreases rapidly with the median SNR of SDSS spectra, reaching measurement-related errors of 0.3 dex or larger for $\text{SNR} < 10$ (e.g., Shen et al. 2011; Rakshit et al. 2020). To reduce the impact of noisy SES measurements on our analysis, in §4 we validate single-epoch photometry using the 54 sources brighter than $r = 21$.

In the right panel of Fig. 1, we display the redshift distribution of these 54 quasars. As we can see, these sources present spectroscopic redshifts between $z \approx 0.5$ and 3.5, which enables testing single-epoch photometry using the lines $\text{H}\beta$, Mg II , and C IV . The maximum redshift for quasar detection in J-PAS is $z \approx 6$; nonetheless, the validation sample does not present any source above $z = 4$ because the miniJPAS survey only observed $\approx 1 \text{ deg}^2$ and the angular number density of quasars brighter than $r = 21$ at $z > 4$ is smaller than 1 per square degree (Palanque-Delabrouille et al. 2013, 2016). Throughout this work, we use SDSS redshift estimates to conduct single-epoch photometry measurements; however, we will not have access to spectroscopic redshifts for the majority of sources that the J-PAS survey will observe. We expect photometric redshifts with subpercent precision for J-PAS quasars (Abramo et al. 2012; Chaves-Montero et al. 2017; Bonoli et al. 2021b); as a result, photometric redshift errors are expected to be a subdominant source of uncertainty for our technique (see Appendix B).

3 MODEL

In this section, we describe our novel approach to measure SMBH masses from single-epoch photometry. We first discuss the theoretical foundations of this method in §3.1, and then we describe our strategy to measure continuum luminosities, emission line properties, and SMBH masses in §3.2, §3.3, and §3.4, respectively. Lastly, we test our methodology using simulated J-PAS photospectra in §3.5.

3.1 Theory preambles

The standard approach to measure SMBH masses at cosmological distances relies on measurements of the virial motion of gas in the BLR. Assuming that the SMBH's gravitational field dominates the

motion of these clouds, we can compute SMBH masses using the virial theorem (e.g., Ho 1999; Wandel et al. 1999):

$$M_{\text{BH}} = f \frac{R_{\text{BLR}}(\Delta V)^2}{G}, \quad (1)$$

where G is the gravitational constant, R_{BLR} indicates the size of the BLR, ΔV refers to the virial velocity of the BLR gas, and f is a dimensionless parameter of order unity that depends on the geometry, kinematics, and inclination of the BLR (see Mejía-Restrepo et al. 2018; Williams et al. 2018, and references therein). In practice, it is standard to estimate the virial velocity using either the FWHM or dispersion of broad emission lines, each of these presenting different advantages and disadvantages (e.g., Shen 2013). Throughout the remainder of this section, we describe a new method to measure SMBH masses from J-PAS photospectra by leveraging the tight correlation between continuum luminosity and BLR size.

3.2 Continuum emission

The size of the BLR region presents a tight correlation with the luminosity of the quasar continuum emission, which is emitted by material in the accretion disk of the SMBH (Abramowicz & Fragile 2013) and it is compatible with a power-law from the optical to the near-UV (e.g., Cristiani & Vio 1990; Vanden Berk et al. 2001). However, measuring the luminosity of the continuum is not straightforward; this is because the apparent continuum of a quasar results from the combination of the power-law continuum and other contributions such as unresolved emission and absorption lines, blended iron lines (e.g., Véron-Cetty et al. 2004), Balmer continuum emission (e.g., Wills et al. 1985), host-galaxy contamination (especially for faint sources, e.g., Shen et al. 2011; Hernán-Caballero et al. 2016), dust reddening (e.g., Hopkins et al. 2004), and photometric errors. To alleviate the impact of these features on measurements of the monochromatic continuum luminosity, we first fit a power-law model to the apparent continuum emission, and then we measure the monochromatic luminosity from the best-fitting model.

To estimate the power-law continuum, we start by selecting a set of rest-frame wavelengths λ_w not presenting strong emission features in their surroundings and sampling observer-frame photospectra in a sufficiently dense fashion up to $z = 5$. We find that the wavelengths $\lambda_w = 1350, 1700, 1800, 2200, 3100, 4000, 4200$, and 5200 \AA satisfy both criteria: these wavelengths present a separation of at least 100 \AA from strong emission lines according to quasar composite spectra (e.g., Vanden Berk et al. 2001) and at least two λ_w fall within the J-PAS wavelength range up to $z \approx 5$. We continue by identifying the J-PAS narrow band with the closest pivot wavelength⁴ to the observer-frame value of each λ_w for every source. Then, we compute the median flux of each selected band and those immediately preceding and succeeding; the resulting values approximate the continuum emission. Note that this approach is largely insensitive to redshift errors perturbing λ_w less than half the width of survey filters (see Appendix B).

Even though the selected λ_w are not close to strong emission features, we find it necessary to apply some corrections to account for the impact of spectral features biasing high the continuum emission. By comparing SDSS spectra and miniJPAS photospectra, we find that the impact of the $\text{O IV]}-\text{Si IV } \lambda\lambda 1397.2, 1402.8$ complex and blends of Fe II line emission redward of the Mg II line is alleviated on average by reducing 10% the flux at $\lambda_w = 1350$ and 3100 \AA ,

⁴ As defined in eq. A11 of Tokunaga & Vacca (2005).

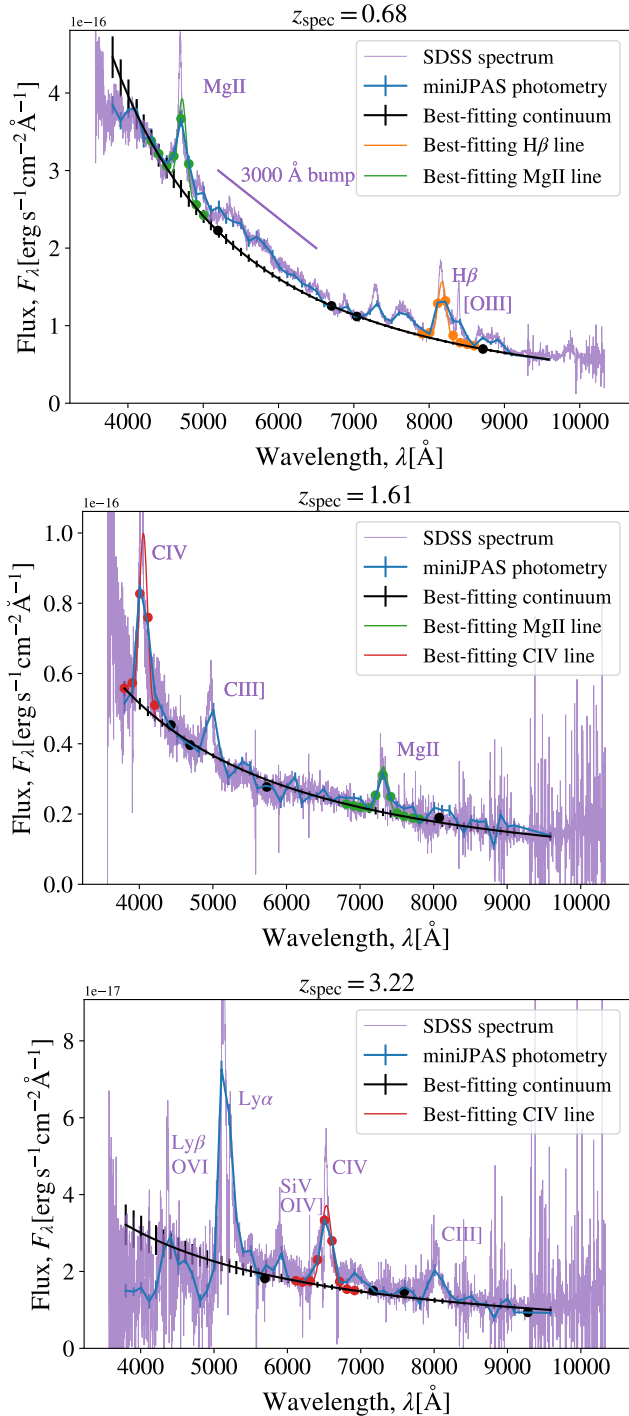


Figure 2. Photometric decomposition of miniJPAS data from 3 SDSS quasars. The top, middle, and bottom panels display the results for a quasar at low, intermediate, and high redshift, respectively. Blue and purple lines show miniJPAS photospectra and SDSS spectra, respectively, black lines display best-fitting continua, and orange, green, and red lines denote best-fitting $H\beta$, $Mg\ II$, and $C\ IV$ emission lines. Error bars show 1σ -equivalent uncertainties. Despite the limited spectral resolution of J-PAS filters, we can readily see that best-fitting lines precisely capture the broad component of quasar emission lines in SDSS spectra.

respectively. Furthermore, we find that reducing 10% the flux at $\lambda_w = 5200\ \text{\AA}$ partially corrects for the change in the continuum slope starting at $\lambda \approx 5000\ \text{\AA}$, which is caused by a combination of host-galaxy contamination and emission from hot dust (see [Vanden Berk et al. 2001](#), and references therein). Both corrections enable a better estimation of the quasar continuum emission from the optical to the near-UV. On the other hand, we do not explicitly correct the quasar continuum for the impact of host-galaxy contamination because the quasars in the validation catalogue are brighter than $r = 21$ and present redshift higher than $z = 0.5$ (see §2.3), and the host-galaxy emission is increasingly weaker for brighter sources at higher redshift (e.g., [Shen et al. 2011](#)). Note that the results are weakly sensitive to all these corrections because we use multiple λ_w to estimate the continuum emission for each source.

We use the publicly available Affine Invariant Markov chain Monte Carlo (MCMC) Ensemble sampler [emcee](#) ([Foreman-Mackey et al. 2013](#))⁵ to compute the best-fitting power-law model to the continuum of each source, $f_{\text{cont}} = f_0 \lambda^{\alpha_\lambda}$, where f_0 and α_λ are the normalisation and spectral index of the power law, respectively. This process works as follows. For each step of the Markov chain, [emcee](#) draws a new value of the previous two parameters, convolves the resulting continuum with the J-PAS filter system, and compares the simulated and actual continuum emission to obtain the likelihood of the selected parameters. We run the code using 100 independent chains of 150 steps, a burn-in phase of 75 steps, and broad uniform priors ($\alpha_\lambda \in [-3.5, 3.5]$). We verify that this configuration results in a robust sampling of the posterior. To determine the best-fitting monochromatic continuum luminosity at a particular wavelength and its error, we first compute the luminosity of the continuum at such wavelength from every accepted step of the MCMC chains. Then, we obtain the best-fitting solution and its uncertainty by computing the median and semi-amplitude of the range enclosing the 16 and 84th percentiles of the resulting values, respectively.

In top, middle, and bottom panels of Fig. 2, we display the photometric decomposition of miniJPAS data from 3 SDSS quasars at $z = 0.68$, 1.61, and 3.22, respectively. The apparent magnitude of these sources is $r = 18.1$, 20.1, and 20.3, their SDSS ID 7339–56722–108, 7339–56722–153, and 7339–56722–147, and their miniJPAS ID 00853, 15867, and 14873. Blue and purple lines show miniJPAS photospectra and SDSS spectra, respectively, black lines display best-fitting quasar continua, and error bars indicate 1σ -equivalent errors. Even though the spectral resolution of narrow-band filters is not high enough to resolve narrow spectral features, we can readily see that miniJPAS photospectra resolve broad emission lines precisely.

We find that the best-fitting continua follow the SDSS-observed continua closely, particularly for wavelengths not contaminated by important spectral features. Black dots indicate the values used to compute the best-fitting continua; as explained above, we select these wavelength intervals because the strongest quasar emission lines do not contaminate their flux. On the other hand, weaker spectral features affect some of these wavelength intervals. In the top panel, the 3000 \AA bump ([Grandi 1982](#); [Oke et al. 1984](#); [Wills et al. 1985](#)) and the change in the continuum slope near $\lambda = 5000\ \text{\AA}$ ([Vanden Berk et al. 2001](#)) modify the flux of the black dots immediately redwards $Mg\ II$ and $H\beta$, respectively; nevertheless, we can readily see that the flux corrections mentioned above alleviate the impact of these features.

⁵ <https://emcee.readthedocs.io/en/stable/>

3.3 Emission lines

Among all quasar emission lines, we are primarily interested in $H\beta$ $\lambda 4861$, $Mg\ II$ $\lambda 2798$, and $C\ IV$ $\lambda 1549$ because these lines present EWs large enough to significantly modify narrow-band photometry and are calibrated to compute SMBH virial masses (e.g., Kaspi et al. 2000, 2005; Vestergaard & Peterson 2006; Shen et al. 2011; Bentz et al. 2013). In addition, we can detect at least one of these lines from the local universe up to $z = 5$ using the J-PAS filter system, which enables continuous estimation of SMBH masses up to such redshift. We proceed to describe our approach to extract the properties of these emission lines.

For each source, we start by identifying the J-PAS bands with pivot wavelengths within the rest-frame intervals $[4700, 5100]\ \text{\AA}$, $[2600, 3000]\ \text{\AA}$, and $[1450, 1630]\ \text{\AA}$ for the analysis of $H\beta$, $Mg\ II$, and $C\ IV$, respectively. The widths of these intervals are $\Delta\lambda \approx 2.5$, 4.3 , and $3.5 \times 10^4\ \text{km s}^{-1}$, which are wide enough to encompass the broadest quasar emission lines almost entirely (e.g., Rakshit et al. 2020). We restrict our analysis to emission lines with observer-frame central wavelength within the interval $[4000, 8900]\ \text{\AA}$ to ensure correct sampling of line wings. Then, we compute the relative difference between the miniJPAS photometry and best-fitting continuum emission for the selected bands (see §3.2), producing a line-only spectrum.

Spectral decomposition methods usually consider multiple broad and narrow components to recover the shape of emission line profiles more precisely (e.g., Greene & Ho 2005; Shen et al. 2011; Guo et al. 2019). However, to avoid degeneracies between different components due to the limited spectral resolution of J-PAS photospectra, we use a single Gaussian to compute the amplitude, centre, and width of each emission line from the line-only spectrum. We do so using the MCMC sampler EMCEE (see also §3.2): for each step of the Markov chain, EMCEE draws a new value for the amplitude, centre, and width of the target emission line, convolves the resulting line with the J-PAS filter system, and compares the simulated line and the line-only spectrum to obtain the likelihood of the selected parameters. For each line, we run the code using 75 independent chains of 500 steps, a burn-in phase of 150 steps, and broad uniform priors. Specifically, we allow the line centre to move as much as an observer-frame distance of $75\ \text{\AA}$ from the rest-frame position of the target line, which corresponds to approximately half the width of a narrow-band J-PAS filter. This wide prior in the line centre aims to accommodate for possible velocity shifts or redshift errors. We compute the best-fitting value and error of line properties following the same strategy as for the continuum luminosity in §3.2.

We find that the $[O\ III]\ \lambda\lambda 4958.9, 5006.8$ complex and blended iron lines hinder the correct estimation of line properties for $H\beta$ and $Mg\ II$, respectively. Spectral methods usually model these features; however, the spectral resolution of J-PAS is too coarse to follow this approach. By comparing SDSS spectra and miniJPAS photospectra, we find that we can mitigate the overall impact of these features on line fits by reducing 50, 50, 25, and 50% the flux of the J-PAS bands with pivot rest-frame wavelength closest to $\lambda = 2700, 2950, 4960$, and $5008\ \text{\AA}$, respectively. The $H\beta$ correction is essential for all sources because the spectral resolution of J-PAS bands is not high enough to resolve $H\beta$ and the $[O\ III]\ \lambda\lambda 4958.9, 5006.8$ complex separately. The $Mg\ II$ correction only improves the results for lines broader than $\sim 8000\ \text{km s}^{-1}$ because for narrower lines the spectral resolution of J-PAS is high enough to resolve $Mg\ II$ and blended iron lines separately. Not introducing these corrections results in overestimating the width of emission lines.

In Fig. 2, we show the best-fitting emission line models to the

broad lines of example quasars. Orange, green, and red colours indicate the results for $H\beta$, $Mg\ II$, and $C\ IV$, respectively, and coloured lines and dots denote best-fitting emission lines and the convolution of these lines with J-PAS filters. By comparing the result of photometric measurements and SDSS spectra, we can readily see that best-fitting lines capture the broad component of $H\beta$, $Mg\ II$, and $C\ IV$ precisely. This level of agreement is remarkable given the significant difference in spectral resolution between SDSS spectra and J-PAS photospectra, with average spectral resolutions of $R \approx 1800$ and 60 (respectively; York et al. 2000; Benitez et al. 2014). The spectral resolution of J-PAS photospectra suggests that we can only resolve lines broader than $\sim 5000\ \text{km s}^{-1}$; however, this calculation does not account for the overlapping of the transmission curve of adjacent J-PAS filters.

3.4 SMBH virial masses

At cosmological distances, the standard approach to compute SMBH masses assumes that the BLR is virialised and that the SMBH gravitational field dominates the motion of gas clouds in this region. Single-epoch spectroscopy computes virial masses by leveraging the tight correlation between continuum luminosity and BLR size (e.g., Kaspi et al. 2000; Bentz et al. 2009)

$$\log\left(\frac{M_{BH}}{M_{\odot}}\right) = A + B \log\left(\frac{\lambda L_{\lambda}}{10^{44}\text{erg s}^{-1}}\right) + 2 \log\left(\frac{FWHM}{\text{km s}^{-1}}\right), \quad (2)$$

where FWHM stands for the full width at half maximum of broad emission lines, λL_{λ} refers to the monochromatic continuum luminosity – typically measured over a spectral region adjacent to the respective broad emission line –, and A and B are virial coefficients calibrated using either sources with both SES and RM measurements (e.g., Kaspi et al. 2000; Bentz et al. 2013) or internally based on the availability of multiple lines for the same source (e.g., McLure & Jarvis 2002; Vestergaard & Peterson 2006; Trakhtenbrot & Netzer 2012; Marinello et al. 2020). We compute $H\beta$ -, $Mg\ II$ -, and $C\ IV$ -based virial masses using the continuum luminosity at $\lambda = 5100, 3000$, and $1350\ \text{\AA}$, respectively, and the same virial coefficients as SDSS-based quasar catalogues (Shen et al. 2011; Rakshit et al. 2020): $A = 0.91$ and $B = 0.50$ for $H\beta$ (Vestergaard & Peterson 2006), $A = 0.74$ and $B = 0.62$ for $Mg\ II$ (Shen et al. 2011; Trakhtenbrot & Netzer 2012), and $A = 0.66$ and $B = 0.53$ for $C\ IV$ (Vestergaard & Peterson 2006). Consequently, SMBH masses depend approximately four times more strongly on FWHM than continuum luminosity measurements.

Different calibrations or spectral decomposition techniques may result in differences as large as 0.4 dex between RM and SES masses (e.g., Collin et al. 2006; Kelly et al. 2009; Shen 2013; Bontà et al. 2020); motivated by this, some works recalibrate virial coefficients using RM and SES measurements from the same spectral decomposition code to reduce these errors. It is also worth noting that the precision of SMBH mass estimates depends on the emission line used during the inference process: $H\beta$ -based masses present a scatter of 0.3 and 0.5 dex relative to $Mg\ II$ - and $C\ IV$ -based masses, respectively (Trakhtenbrot & Netzer 2012).

To compute single-epoch photometry masses, we use continuum luminosities and line widths estimated from J-PAS photospectra (see §3.2 and §3.3, respectively). Ideally, we would recalibrate Eq. 2 coefficients using sources presenting both RM and SEP mass measurements; however, miniJPAS did not observe any quasar with RM measurements. In §4, we resort to recalibrating these coefficients using sources with both single-epoch spectroscopic and photometric measurements; to do so, we use the gradient-based BFGS

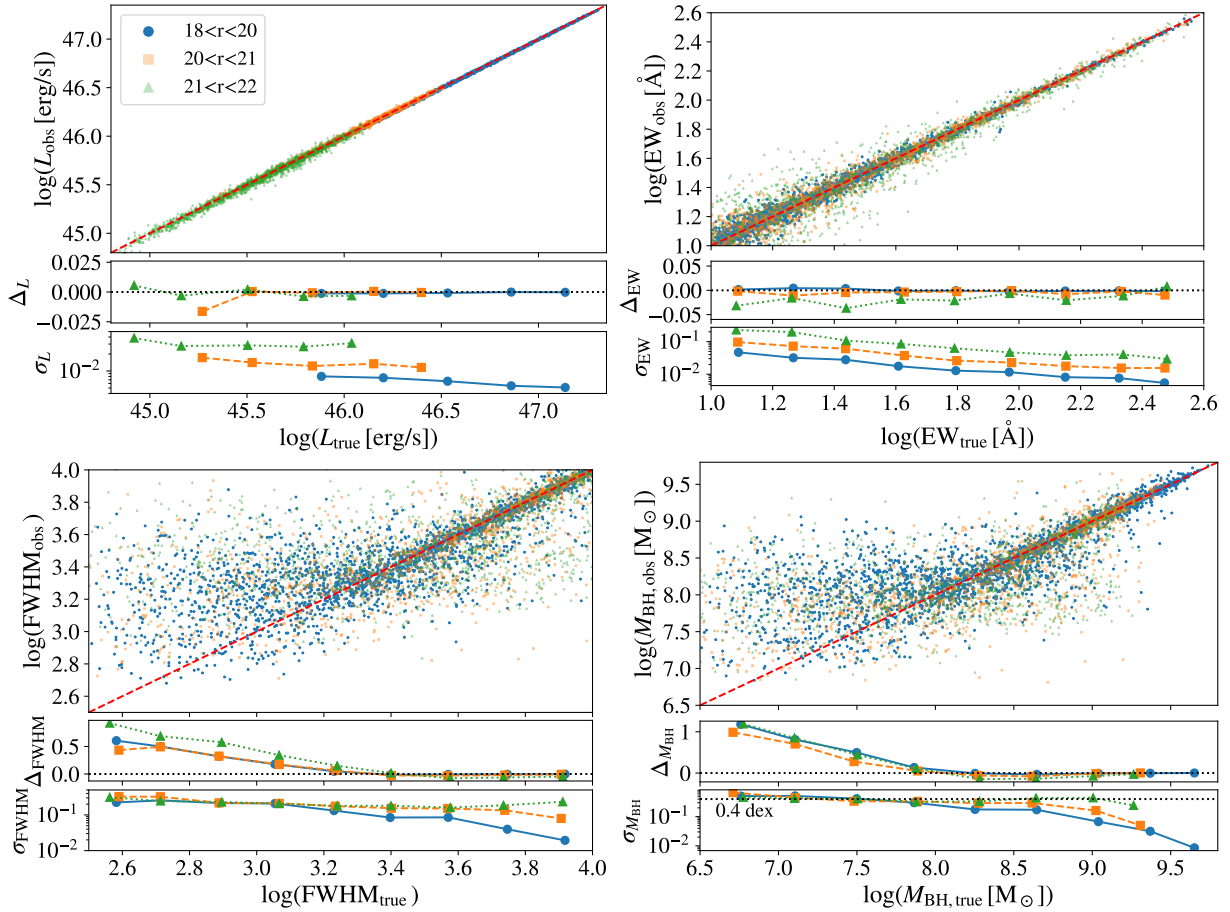


Figure 3. Single-epoch photometry measurements of λL_{λ} (1350 Å) continuum luminosity (top-left panel), C iv EW (top-right panel), C iv FWHM (bottom-left panel), and C iv-based SMBH mass (bottom-right panel) from simulated J-PAS sources. Blue dots, orange squares, and green triangles show the results for sources with $18 < r < 20$, $20 < r < 21$, and $21 < r < 22$, respectively, and red dashed lines indicate a one-to-one relation between actual and measured properties. Middle and bottom subpanels display the mean and standard deviation of the logarithmic difference between actual and measured properties. We find that our method yields unbiased FWHM measurements only for lines broader than $\approx 1500 \text{ km s}^{-1}$ due to the limited spectral resolution of J-PAS photospectra, which prevents us from measuring the mass of sources with $\log(M_{\text{BH}}/M_{\odot}) \lesssim 8$ in an unbiased fashion. We find similar results for H β and Mg II.

algorithm (Broyden 1970; Fletcher 1970; Goldfarb 1970; Shanno & Kettler 1970) implemented in `scipy` (Virtanen et al. 2020). This recalibration has two important benefits: it absorbs systematic differences between spectroscopic and photometric measurements of both continuum luminosity, which may be caused by over- or underestimating the correction from aperture to total magnitudes (see §2.3), and line widths, which may appear due to the different number of components used to fit line profiles (see §3.3).

3.5 Tests using idealised simulations

In order to thoroughly test our methodology, we proceed to study the feasibility of using single-epoch photometry to measure SMBH masses using simulated observations of J-PAS quasars.

Modelling the spectral energy distribution of a quasar is challenging due to correlations between multiple quasar properties (e.g., Baldwin 1977; Dong et al. 2009; Shen et al. 2011), the presence of a panoply of weak and blended emission lines (e.g., Davidson & Netzer 1979), the complex profile of some broad emission lines (e.g., Nagao et al. 2006; Shen et al. 2011; Kollatschny & Zetzl 2013), the diversity of quasar continua (e.g., Jensen et al. 2016), emission line velocity shifts (e.g., Richards et al. 2011; Shen et al. 2016), and

host-galaxy contamination (e.g., Vanden Berk et al. 2001). Instead of accounting for all these effects, we proceed to generate idealised quasar observations by modelling the quasar continuum emission as a power-law and each broad emission line as a single Gaussian. This approach ensures that the only sources of uncertainty affecting SEP masses are the limited resolution of the J-PAS filter system and the level of photometric errors expected for this survey. In §4, we study the aggregated impact of all the aforementioned effects and others such as variability by comparing single-epoch spectroscopy and photometry measurements from quasars in the miniJPAS validation sample (§2.3).

For each source, we first model the continuum emission using a power-law of index $\alpha_{\lambda} = -1.56$, which provides an excellent fit to the quasar continuum emission from Ly α to H β (Vanden Berk et al. 2001). Then, we add the emission lines H β , Mg II, and C iv to the continuum emission, which we model using a single Gaussian function with the same width. After that, we redshift the resulting spectral energy distribution from rest- to observer-frame, and we convolve it with the J-PAS filter system. Finally, we perturb mock photospectra according to the level of photometric uncertainties expected for the J-PAS survey (Benítez et al. 2014). In summary, four free parameters characterise each simu-

lated photospectra: continuum r -band magnitude, rest-frame EW, FWHM, and redshift. To generate mock observations, we first draw 10 500 random combinations of these parameters within the intervals $z \in [0.01, 4.50]$, $r \in [18, 23]$, $\log(\text{EW}/\text{\AA}) \in [1, 2.6]$, and $\log(\text{FWHM}/\text{km s}^{-1}) \in [2.5, 4.0]$ using Latin Hypercube sampling (McKay et al. 1979). Then, we follow the previously-mentioned strategy to generate a J-PAS photospectra for each combination of parameters.

In Figure 3, we compare the SEP measurements from mock photospectra and the input quantities used to simulate these. Note that we analyse mock observations using a slightly modified version of the model described in §3: we do not apply any correction to either the continuum emission or emission lines because simulated photospectra do not incorporate any contaminant. Blue dots, orange squares, and green triangles indicate the results for sources with $18 < r < 20$, $20 < r < 21$, and $21 < r < 22$, respectively, and red dashed lines indicate the 1:1 relations between input and measured quantities. In each panel, the middle and bottom subpanels display the mean and standard deviation of the logarithmic difference between input and measured values. As expected, the precision of all measurements is increasingly larger for brighter sources as the relative impact of the associated photometric errors decreases.

In the top-left and top-right panels, we display measurements of the monochromatic continuum luminosity at 1350 Å and the EW of C iv, respectively. As we can see, the precision of the measurements increases for more luminous sources and stronger lines; this is because the relative impact of photometric errors decreases with both the brightness of the continuum and the strength of emission lines. We also find that our model only delivers unbiased measurements for sources brighter than $r \simeq 21$; motivated by this, we only consider sources brighter than such magnitude to estimate the performance of single-epoch photometry in §4.

In the bottom-left panel, we show measurements of the FWHM of C iv. We find that the precision of these measurements increases for broader lines; this is because the J-PAS filter system resolves wider lines with a larger number of bands. The most prominent feature of this panel is that FWHM measurements display a systematic bias for emission lines narrower than $\approx 1500 \text{ km s}^{-1}$. We can understand this trend in terms of the limited spectral resolution of the J-PAS filter system: on average, emission lines narrower than $\approx 1500 \text{ km s}^{-1}$ perturb the flux of a single J-PAS band, which causes a complete degeneracy between the amplitude and FWHM of the best-fitting line. For such lines, our method delivers practically any result between the actual width and the minimum one resolvable, thereby biasing high FWHM measurements. In Appendix A, we show that backward-modelling observations result in systematic biases even for lines as wide as $\approx 10\,000 \text{ km s}^{-1}$; therefore, forward-modelling quasar observations enables us to push this limit by almost an order of magnitude. Note that our naive estimate for the width of the narrowest line resolvable by J-PAS is approximately 3 times larger than the actual value (see §3.3).

In the bottom-right panel, we display measurements of C iv-based SMBH mass. Note that we compute SMBH masses using the virial coefficients quoted in §3.4. As we can see, our method yields unbiased masses only for sources with $\log(M_{\text{BH}}/M_{\odot}) \gtrsim 8$, reflecting the biased FWHM measurements for lines narrower than $\approx 1500 \text{ km s}^{-1}$. For sources with FWHM larger than the aforementioned threshold, we find that SEP masses show no systematic bias and that the precision of these ranges from 0.4 to 0.01 dex for SMBH with masses from $\log(M_{\text{BH}}/M_{\odot}) \approx 8$ to 9.75, respectively. We also find that the precision of these measurements increases with the SMBH mass for sources brighter than $r = 21$, which is explained by

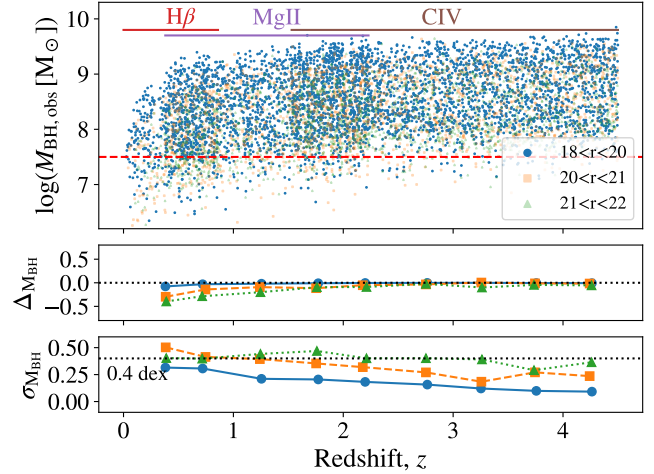


Figure 4. Single-epoch photometry masses from simulated J-PAS observations of sources with actual SMBH mass larger than $\log(M_{\text{BH}}/M_{\odot}) = 7.5$. The red dashed line indicates this threshold. As we can see, the combination of H β , Mg II, and C IV enables measuring SMBH masses from $z = 0$ to 5 continuously.

the increasing precision of both continuum luminosity and FWHM measurements for sources with brighter continua and broader lines. Note that we find similar results for H β - and Mg II-based measurements.

In Fig. 4, we display SEP mass measurements from H β , Mg II, and C IV as a function of redshift. As we can see, these lines enable measuring SMBH masses from $z = 0$ to 5 continuously. We only display results for sources with an actual mass larger than $\log(M_{\text{BH}}/M_{\odot}) = 7.5$; we set this threshold to understand better the impact of the limited resolution of the J-PAS filter system on measurements for low mass sources. We find that our model yields unbiased SMBH masses for sources with both $r < 20$ and $\log(M_{\text{BH}}/M_{\odot}) > 7.5$ across the whole redshift range. On the other hand, sources with $r > 20$ present slightly biased masses below $z = 1$, especially those with less massive SMBHs. This is due to the combination of two effects: the precision of SEP measurements increases with both apparent magnitude and line width, and at fixed FWHM (in km s^{-1}), the observer-frame line width (in Å) grows with redshift as $1 + z$. We check that our model yields unbiased SMBH mass estimates for sources with emission lines broader than an observer-frame width of FWHM = 30 Å.

4 RESULTS

In §3, we describe single-epoch photometry and we validate our methodology using simulated J-PAS photospectra. In this section, we characterise the precision of this technique by comparing single-epoch photometry and spectroscopy measurements for 54 SDSS quasars observed by the miniJPAS survey (see §2.3). In §4.1, 4.2, and 4.3, we show the results for continuum luminosities, emission line properties, and SMBH virial masses, respectively, and we gather these in Table 1.

4.1 Continuum luminosity

In Fig. 5, we display continuum luminosity measurements from SDSS spectra and miniJPAS photospectra for the 54 quasars in the

Table 1. Single-epoch photometry measurements for sources in the miniJPAS validation catalogue. An extended version of this table also containing single-epoch spectroscopy measurements can be found [here](#).

ID [†]	z	r	$\log(L_\lambda [\text{erg/s}])$			$\log(\text{FWHM} [\text{km s}^{-1}])$			$\log(M_{\text{BH}} [M_\odot])$		
			5100 Å	3000 Å	1350 Å	H β	Mg II	C IV	H β	Mg II	C IV
19320	0.482	20.0	44.16 ^{+0.03} _{-0.03}	44.23 ^{+0.02} _{-0.02}	—	3.81 ^{+0.29} _{-0.37}	3.61 ^{+0.52} _{-0.55}	—	8.53 ± 0.66	7.65 ± 1.06	—
1234	0.531	20.6	44.10 ^{+0.04} _{-0.04}	43.86 ^{+0.04} _{-0.04}	—	3.91 ^{+0.15} _{-0.36}	3.87 ^{+0.18} _{-0.16}	—	8.73 ± 0.51	7.94 ± 0.34	—
8820	0.548	20.0	44.32 ^{+0.03} _{-0.03}	44.29 ^{+0.04} _{-0.04}	—	3.87 ^{+0.18} _{-0.38}	3.74 ^{+0.24} _{-0.23}	—	8.71 ± 0.56	7.94 ± 0.49	—
915	0.600	20.9	44.32 ^{+0.05} _{-0.05}	43.74 ^{+0.04} _{-0.07}	—	3.60 ^{+0.47} _{-0.75}	4.08 ^{+0.23} _{-0.25}	—	8.16 ± 1.22	8.30 ± 0.47	—
1126	0.602	20.0	44.39 ^{+0.02} _{-0.02}	44.45 ^{+0.02} _{-0.02}	—	3.91 ^{+0.13} _{-0.16}	4.03 ^{+0.11} _{-0.13}	—	8.81 ± 0.29	8.62 ± 0.24	—
8427	0.647	19.2	44.78 ^{+0.02} _{-0.02}	44.89 ^{+0.02} _{-0.02}	—	3.80 ^{+0.18} _{-0.28}	3.83 ^{+0.26} _{-0.52}	—	8.67 ± 0.46	8.47 ± 0.78	—
853	0.676	18.0	45.21 ^{+0.02} _{-0.02}	45.48 ^{+0.02} _{-0.02}	—	3.72 ^{+0.10} _{-0.17}	3.86 ^{+0.24} _{-0.24}	—	8.62 ± 0.28	8.89 ± 0.90	—
16055	0.676	20.2	44.47 ^{+0.04} _{-0.04}	44.45 ^{+0.05} _{-0.05}	—	3.65 ^{+0.38} _{-0.73}	3.85 ^{+0.69} _{-0.82}	—	8.31 ± 1.11	8.26 ± 1.29	—
628	0.719	20.0	44.51 ^{+0.04} _{-0.04}	44.61 ^{+0.03} _{-0.03}	—	3.83 ^{+0.26} _{-0.84}	3.59 ^{+0.61} _{-0.58}	—	8.66 ± 1.10	7.84 ± 1.18	—
4846	0.808	20.9	44.46 ^{+0.04} _{-0.04}	44.36 ^{+0.03} _{-0.03}	—	3.48 ^{+0.50} _{-0.68}	4.09 ^{+0.21} _{-0.49}	—	7.96 ± 1.18	8.67 ± 0.70	—
14405	0.825	20.7	44.38 ^{+0.05} _{-0.05}	44.38 ^{+0.04} _{-0.04}	—	3.55 ^{+0.42} _{-0.39}	3.54 ^{+0.24} _{-0.24}	—	8.07 ± 0.81	7.60 ± 0.42	—
3844	0.884	20.5	—	44.52 ^{+0.02} _{-0.02}	—	—	3.87 ^{+0.14} _{-0.23}	—	—	8.34 ± 0.37	—
9169	0.897	20.3	—	44.68 ^{+0.03} _{-0.03}	—	—	4.09 ^{+0.16} _{-0.25}	—	—	8.88 ± 0.41	—
9188	0.986	20.8	—	44.49 ^{+0.04} _{-0.04}	—	—	4.05 ^{+0.14} _{-0.18}	—	—	8.67 ± 0.32	—
18457	0.986	20.3	—	44.75 ^{+0.02} _{-0.02}	—	—	3.71 ^{+0.28} _{-0.33}	—	—	8.16 ± 0.46	—
468	1.002	20.5	—	44.71 ^{+0.03} _{-0.03}	—	—	3.89 ^{+0.33} _{-0.51}	—	—	8.50 ± 0.84	—
13263	1.086	20.8	—	44.65 ^{+0.03} _{-0.02}	—	—	3.99 ^{+0.17} _{-0.28}	—	—	8.66 ± 0.45	—
13691	1.194	19.5	—	45.29 ^{+0.02} _{-0.02}	—	—	4.01 ^{+0.09} _{-0.19}	—	—	9.08 ± 0.19	—
4230	1.213	18.7	—	45.64 ^{+0.01} _{-0.01}	—	—	3.94 ^{+0.10} _{-0.21}	—	—	9.14 ± 0.35	—
11324	1.223	20.8	—	44.73 ^{+0.05} _{-0.04}	—	—	4.13 ^{+0.12} _{-0.13}	—	—	8.98 ± 0.25	—
12523	1.269	20.1	—	45.20 ^{+0.02} _{-0.02}	—	—	3.76 ^{+0.24} _{-0.46}	—	—	8.52 ± 0.70	—
3062	1.286	17.8	—	46.03 ^{+0.01} _{-0.01}	—	—	4.04 ^{+0.05} _{-0.05}	—	—	9.57 ± 0.11	—
5992	1.391	19.9	—	45.31 ^{+0.02} _{-0.03}	—	—	3.78 ^{+0.22} _{-0.31}	—	—	8.62 ± 0.53	—
5491	1.394	19.1	—	45.61 ^{+0.02} _{-0.02}	—	—	3.49 ^{+0.31} _{-0.39}	—	—	8.22 ± 0.70	—
14254	1.492	19.7	—	45.44 ^{+0.03} _{-0.02}	—	—	4.09 ^{+0.12} _{-0.19}	—	—	9.33 ± 0.29	—
8781	1.514	18.7	—	45.86 ^{+0.02} _{-0.02}	—	—	3.99 ^{+0.10} _{-0.13}	—	—	9.37 ± 0.24	—
15615	1.515	20.7	—	45.07 ^{+0.05} _{-0.04}	—	—	4.05 ^{+0.15} _{-0.15}	—	—	9.01 ± 0.29	—
13393	1.584	19.3	—	45.65 ^{+0.03} _{-0.03}	45.96 ^{+0.02} _{-0.02}	—	4.04 ^{+0.09} _{-0.09}	3.57 ^{+0.27} _{-0.27}	—	9.33 ± 0.19	8.55 ± 0.54
15867	1.605	20.0	—	45.43 ^{+0.03} _{-0.03}	45.62 ^{+0.03} _{-0.03}	—	3.83 ^{+0.18} _{-0.18}	3.64 ^{+0.19} _{-0.19}	—	8.80 ± 0.41	8.60 ± 0.39
12132	1.647	19.6	—	45.54 ^{+0.03} _{-0.03}	45.86 ^{+0.03} _{-0.03}	—	4.00 ^{+0.11} _{-0.11}	3.70 ^{+0.28} _{-0.33}	—	9.20 ± 0.22	8.79 ± 0.61
9749	1.674	20.8	—	45.05 ^{+0.12} _{-0.12}	45.23 ^{+0.10} _{-0.10}	—	4.06 ^{+0.15} _{-0.40}	3.97 ^{+0.27} _{-0.42}	—	9.03 ± 0.55	9.16 ± 0.69
11608	1.685	20.3	—	45.41 ^{+0.04} _{-0.04}	45.51 ^{+0.03} _{-0.03}	—	3.89 ^{+0.12} _{-0.16}	4.18 ^{+0.05} _{-0.06}	—	8.91 ± 0.28	9.64 ± 0.11
12363	1.728	20.6	—	45.15 ^{+0.08} _{-0.08}	45.49 ^{+0.03} _{-0.03}	—	3.92 ^{+0.37} _{-0.37}	3.63 ^{+0.35} _{-0.35}	—	8.80 ± 0.62	8.56 ± 0.69
2056	1.743	19.8	—	45.58 ^{+0.03} _{-0.03}	45.79 ^{+0.03} _{-0.03}	—	4.10 ^{+0.11} _{-0.15}	3.82 ^{+0.22} _{-0.37}	—	9.43 ± 0.26	9.00 ± 0.59
2837	1.862	20.2	—	45.60 ^{+0.05} _{-0.05}	45.39 ^{+0.05} _{-0.05}	—	3.72 ^{+0.41} _{-0.80}	4.17 ^{+0.24} _{-0.71}	—	8.68 ± 1.21	9.60 ± 0.95
12352	1.902	20.3	—	45.41 ^{+0.05} _{-0.05}	45.65 ^{+0.02} _{-0.02}	—	3.51 ^{+0.45} _{-0.39}	3.79 ^{+0.09} _{-0.08}	—	8.15 ± 0.84	8.90 ± 0.16
13467	1.902	19.7	—	45.74 ^{+0.03} _{-0.03}	45.84 ^{+0.02} _{-0.02}	—	3.84 ^{+0.22} _{-0.57}	3.64 ^{+0.22} _{-0.29}	—	9.00 ± 0.78	8.65 ± 0.51
14404	1.960	20.2	—	45.58 ^{+0.03} _{-0.03}	45.73 ^{+0.02} _{-0.02}	—	3.78 ^{+0.24} _{-0.53}	4.05 ^{+0.06} _{-0.07}	—	8.78 ± 0.77	9.45 ± 0.13
13090	1.963	20.5	—	45.38 ^{+0.04} _{-0.04}	45.62 ^{+0.02} _{-0.02}	—	3.98 ^{+0.13} _{-0.16}	3.73 ^{+0.19} _{-0.24}	—	9.07 ± 0.29	8.78 ± 0.43
6718	2.003	20.3	—	45.52 ^{+0.04} _{-0.04}	45.63 ^{+0.03} _{-0.03}	—	3.94 ^{+0.11} _{-0.13}	3.95 ^{+0.14} _{-0.25}	—	9.06 ± 0.24	9.23 ± 0.39
14602	2.031	20.2	—	45.66 ^{+0.02} _{-0.03}	45.60 ^{+0.02} _{-0.02}	—	4.11 ^{+0.08} _{-0.12}	4.01 ^{+0.07} _{-0.06}	—	9.49 ± 0.20	9.34 ± 0.13
5085	2.033	20.3	—	45.45 ^{+0.04} _{-0.04}	45.70 ^{+0.04} _{-0.03}	—	4.07 ^{+0.09} _{-0.10}	3.75 ^{+0.16} _{-0.18}	—	9.28 ± 0.19	8.83 ± 0.34
17351	2.041	20.2	—	45.54 ^{+0.03} _{-0.03}	45.70 ^{+0.03} _{-0.03}	—	3.86 ^{+0.24} _{-0.32}	3.59 ^{+0.48} _{-0.52}	—	8.93 ± 0.56	8.52 ± 1.00
1224	2.305	20.2	—	—	45.81 ^{+0.05} _{-0.05}	—	—	3.95 ^{+0.11} _{-0.12}	—	—	9.26 ± 0.23
2363	2.306	19.4	—	—	46.17 ^{+0.02} _{-0.02}	—	—	4.07 ^{+0.08} _{-0.09}	—	—	9.61 ± 0.17
4455	2.351	20.9	—	—	45.58 ^{+0.07} _{-0.07}	—	—	4.08 ^{+0.16} _{-0.22}	—	—	9.48 ± 0.37
11608	2.463	18.3	—	—	46.63 ^{+0.02} _{-0.02}	—	—	3.95 ^{+0.07} _{-0.08}	—	—	9.49 ± 0.15
3755	2.581	19.7	—	—	46.10 ^{+0.02} _{-0.02}	—	—	3.85 ^{+0.12} _{-0.29}	—	—	9.15 ± 0.41
4342	2.591	19.9	—	—	46.02 ^{+0.02} _{-0.02}	—	—	4.11 ^{+0.06} _{-0.07}	—	—	9.64 ± 0.14
4481	2.594	20.0	—	—	45.99 ^{+0.02} _{-0.02}	—	—	3.96 ^{+0.09} _{-0.11}	—	—	9.34 ± 0.20
12507	2.631	18.6	—	—	46.51 ^{+0.02} _{-0.02}	—	—	4.05 ^{+0.10} _{-0.10}	—	—	9.66 ± 0.22
12752	3.043	20.1	—	—	46.04 ^{+0.03} _{-0.03}	—	—	3.78 ^{+0.11} _{-0.14}	—	—	9.00 ± 0.25
20297	3.194	20.9	—	—	45.77 ^{+0.05} _{-0.05}	—	—	3.63 ^{+0.23} _{-0.24}	—	—	8.62 ± 0.47
14873	3.217	20.1	—	—	46.08 ^{+0.04} _{-0.04}	—	—	3.90 ^{+0.08} _{-0.09}	—	—	9.24 ± 0.17

[†]ID in the miniJPAS catalogue.

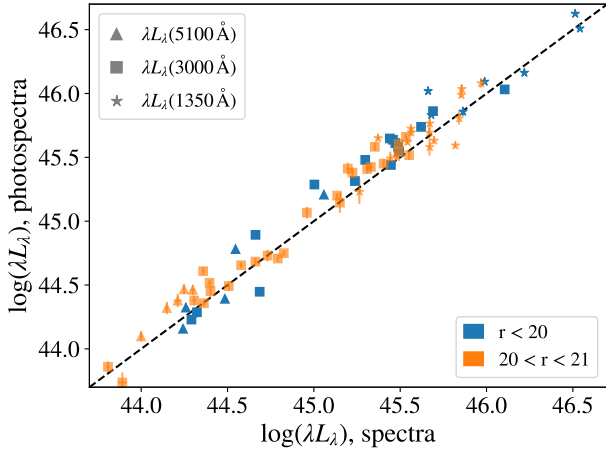


Figure 5. Continuum luminosity measurements from SDSS spectra and miniJPAS photospectra. Triangles, squares, and stars indicate the continuum luminosity at $\lambda = 5100, 3000$, and 1350 \AA , respectively, and blue and orange symbols display the results for sources with $r < 20$ and $20 < r < 21$, error bars denote 1σ -equivalent uncertainties, and the dashed line indicates a 1:1 relation between SES and SEP measurements.

validation sample. Triangles, squares, and stars indicate the continuum luminosity at $\lambda = 5100, 3000$, and 1350 \AA , respectively, and blue and orange symbols display the results for sources with $r < 20$ and $20 < r < 21$, and the dashed line indicates a 1:1 relation between SES and SEP measurements. Error bars denote 1σ -equivalent uncertainties from spectral and photometric decomposition. As we can see, these uncertainties do not capture the dispersion of measurements between SDSS spectra and miniJPAS photospectra; this is likely because error bars do not attempt to capture the impact of variability on the results, which is an important source on uncertainty in the comparison between spectroscopic and photometric measurements (see §2.3).

We find a small systematic difference between photometric and spectroscopic measurements: the mean and standard deviation of their difference are -0.11 and 0.11 dex for $\lambda L_{\lambda}(5100 \text{ \AA})$, -0.07 and 0.11 dex for $\lambda L_{\lambda}(3000 \text{ \AA})$, and -0.07 and 0.12 dex for $\lambda L_{\lambda}(1350 \text{ \AA})$. We check that this bias is sensitive to the photometric correction used to convert aperture to total magnitudes (see §2.3), and that it disappears by slightly decreasing such correction. Nonetheless, it is crucial to keep in mind that a constant bias has negligible impact on the computation of SMBH masses because the recalibration of virial coefficients absorbs it (see §3.4).

4.2 Emission line properties

In Fig. 6, we display EW (top row) and FWHM (bottom row) measurements from SDSS spectra and miniJPAS photospectra for the 54 quasars in the validation sample. The left, middle, and right panels show the results for $H\beta$, $Mg \text{ II}$, and $C \text{ IV}$, respectively. These lines are broader than 1500 km s^{-1} for all sources, and thus we expect accurate FWHM measurements from miniJPAS photospectra (see §3.5). The symbol ρ indicates the Pearson correlation coefficient between spectroscopic and photometric measurements. As we can see, EWs and FWHM present much larger error bars than continuum luminosity measurements, reflecting the complexity of extracting line properties. The median precision of EW and FWHM measurements from photometric data is 16 and 30%, respectively, and from spectroscopic data is 6 and 8%. Therefore, at fixed r -band

apparent magnitude, spectroscopic measurements from SDSS are between 2 to 4 times more precise than photometric measurements from miniJPAS. Note that these error bars do not attempt to capture the impact of variability on the comparison between spectroscopic and photometric measurements (see §2.3).

We find that the Person correlation coefficient between spectroscopic and photometric FWHM measurements is almost unity for $H\beta$, close to $\rho = 0.5$ for $C \text{ IV}$, and approximately $\rho = 0.3$ for $Mg \text{ II}$. The modest value of the correlation coefficient for some lines is likely caused by the combination of the limited SNR of observations quasar variability. Nonetheless, the agreement between emission line properties from spectroscopic and photometric measurements is substantial: we find that the mean and standard deviation of the difference for EWs are 0.15 and 0.36 dex for $H\beta$, -0.07 and 0.19 dex for $Mg \text{ II}$, and 0.09 and 0.17 dex for $C \text{ IV}$, and for FWHM -0.06 and 0.09 dex for $H\beta$, -0.28 and 0.19 dex for $Mg \text{ II}$, and -0.20 and 0.18 dex for $C \text{ IV}$. We thus find a systematic difference between FWHM measurements from SDSS spectra and miniJPAS photospectra, possibly because we use a single component to fit line profiles while Rakshit et al. (2020) does so using multiple components (see §3.3). Note that differences of the same order are found between widths measured by spectral decomposition methods using a single and multiple components (e.g., Shen et al. 2011; Rakshit et al. 2020). However, it is essential to notice that a constant bias has a negligible impact on the computation of SMBH masses because the recalibration of virial coefficients absorbs it (see §3.4).

4.3 SMBH virial masses

Before computing SMBH virial masses, we recalibrate the virial coefficients of Eq. 2 to correct for possible systematic differences between single-epoch spectroscopy and photometry measurements due to the different methodologies to compute continuum luminosities and emission line properties. Following the approach explained in §3.4, we find $A = 0.876 \pm 0.005$ and $B = 0.263 \pm 0.013$ for $H\beta$, $A = 0.292 \pm 0.017$ and $B = 0.590 \pm 0.006$ for $Mg \text{ II}$, and $A = 0.894 \pm 0.125$ and $B = 0.263 \pm 0.029$ for $C \text{ IV}$.

In Figure 7, we compare different SMBH mass estimates for quasars in the validation sample: SEP masses from miniJPAS photospectra produced using the previous coefficients and SES masses from SDSS spectra generated using the coefficients quoted in §3.4. The middle and bottom subpanels show the mean and standard deviation of the logarithmic difference between spectroscopic and photometric measurements, respectively, dashed lines indicate a 1:1 relation between these measurements, and dotted lines are displaced by 0.4 dex from such relationship. Horizontal error bars denote 1σ uncertainties for SES masses, which are computed via error propagation of Eq. 2 (see Rakshit et al. 2020). We compute error bars for SEP masses following the previous approach for a fair comparison between spectroscopic and photometric error estimates. As we can see, the size of error bars decreases with the mass of the sources for both techniques, reflecting the increasingly larger precision of measurements for brighter sources, and at fixed apparent magnitude, for sources with broader lines (see §3.4). Note that error bars do not capture the impact of systematic uncertainties affecting single-epoch masses.

We find that single-epoch photometry and spectroscopy masses display a remarkable agreement, with no systematic difference between these and most measurements less than 1σ away from the 1:1 relation. We can thus conclude that single-epoch photometry delivers unbiased measurements of SMBH masses despite the limited spectral resolution of J-PAS photospectra. We also find that

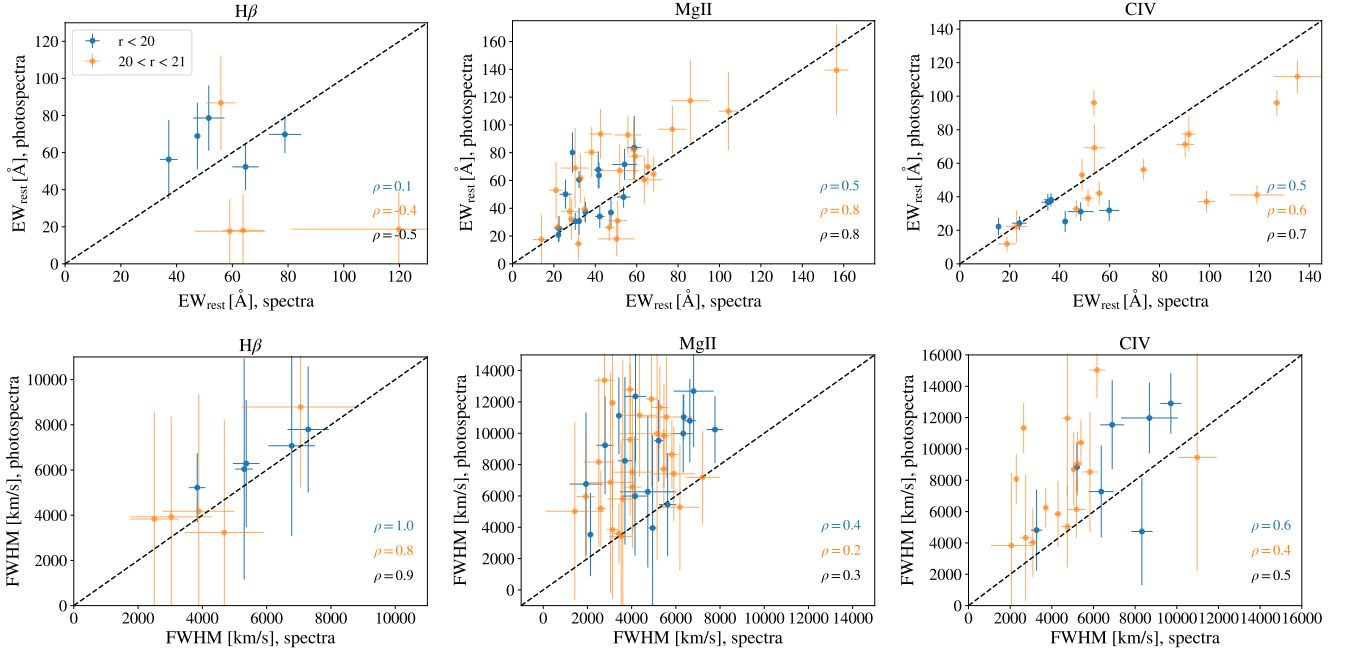


Figure 6. EW (top row) and FWHM (bottom row) measurements from SDSS spectra and miniJPAS photospectra. The left, middle, and right panels show the results for H β , Mg II, and C IV, respectively. Dashed lines indicate a 1:1 relation between photometric and spectroscopic measurements. The symbol ρ indicates the Pearson correlation coefficient between spectroscopic and photometric measurements.

the standard deviation of the difference between spectroscopic and photometric measurements decreases with the mass of the sources: it ranges from 0.4 to 0.07 dex for SMBHs with masses from $\log(M_{\text{BH}}/M_{\odot}) \approx 8$ to 9.75, respectively. This level of precision is in line with our forecasts from simulated miniJPAS observations (see §3.5), suggesting limited impact unresolved emission lines, host-galaxy contamination, and other effects on continuum luminosity and emission line properties (see §3.2 and 3.3).

An important consideration is that single-epoch photometry faces similar systematic uncertainties as single-epoch spectroscopy, including the chosen measurement that characterises line widths, different assumptions involving spectral decomposition methods, host-galaxy contamination, broad absorption lines, outflows, residual dependence of SMBH masses on the Eddington ratio, uncertainties in the relation between continuum luminosity and BLR size, variations of the virial factor with the BLR geometry, and possible non reverberating components of some emission lines (for a recent detailed discussion about these effects see Bontà et al. 2020). The aforementioned effects induce differences of the order of 0.4 dex between RM and SES masses, with little dependence on SMBH mass (e.g., Grier et al. 2019; Homayouni et al. 2020; Bontà et al. 2020). If we assume that the impact of the previous systematics on single-epoch spectroscopy and photometry is of the same order, we can compare the precision of these techniques measuring SMBH masses. For SMBHs with masses of the order of $\log(M_{\text{BH}}/M_{\odot}) = 8$, the standard deviation of the difference between SES and SEP masses is of the same order as the impact of systematic uncertainties, suggesting that SEP masses are $\sqrt{2} \approx 1.4$ times less precise than SES masses. Systematic uncertainties progressively dominate the error budget for SMBH with larger masses; for sources with $\log(M_{\text{BH}}/M_{\odot}) \approx 9.0$ and 9.5, SES masses are only 12 and 3% more precise than SEP masses, respectively. We can thus conclude that single-epoch photometry yields SMBH virial masses with only mildly worse precision than single-epoch spectroscopy

for the majority of sources in the validation sample. However, a more thorough study of the accuracy of single-epoch photometry requires sources with both RM and SEP masses.

5 CONCLUSIONS

Precise measurements of SMBH masses are crucial to characterise the properties of the SMBH population, understand the links between SMBHs and their host galaxies, and use quasars as large-scale structure tracers for multiple cosmological applications. In this work, we develop a novel approach to measure SMBH virial masses from single-epoch, narrow-band photometric observations. We summarise our main findings as follows:

- In §3, we describe a Bayesian-based approach to measure continuum luminosities and emission line properties from narrow-band photometric data. We validate our methodology using simulated J-PAS observations, finding that they can deliver accurate continuum luminosities for sources brighter than $r = 21$ and unbiased FWHM measurements for lines broader than $\approx 1500 \text{ km s}^{-1}$. For the kind of quasars we consider here, this value translates into a minimum SMBH mass of approximately $\log(M_{\text{BH}}/M_{\odot}) = 8$.
- In §4, we characterise the performance of our methodology using 54 SDSS quasars observed by the miniJPAS survey, a proof-of-concept project of the J-PAS collaboration covering $\approx 1 \text{ deg}^2$ of the northern sky using the 56 J-PAS narrow-band filters. We find that the standard deviation of the difference between single-epoch spectroscopy measurements from SDSS and single-epoch photometry measurements from miniJPAS is approximately 0.1 and 0.2 dex for continuum luminosities and FWHM, respectively. However, we caution that quasar variability is a significant source of uncertainty for this comparison.
- In Fig. 7, we compare SES masses from SDSS and SEP masses

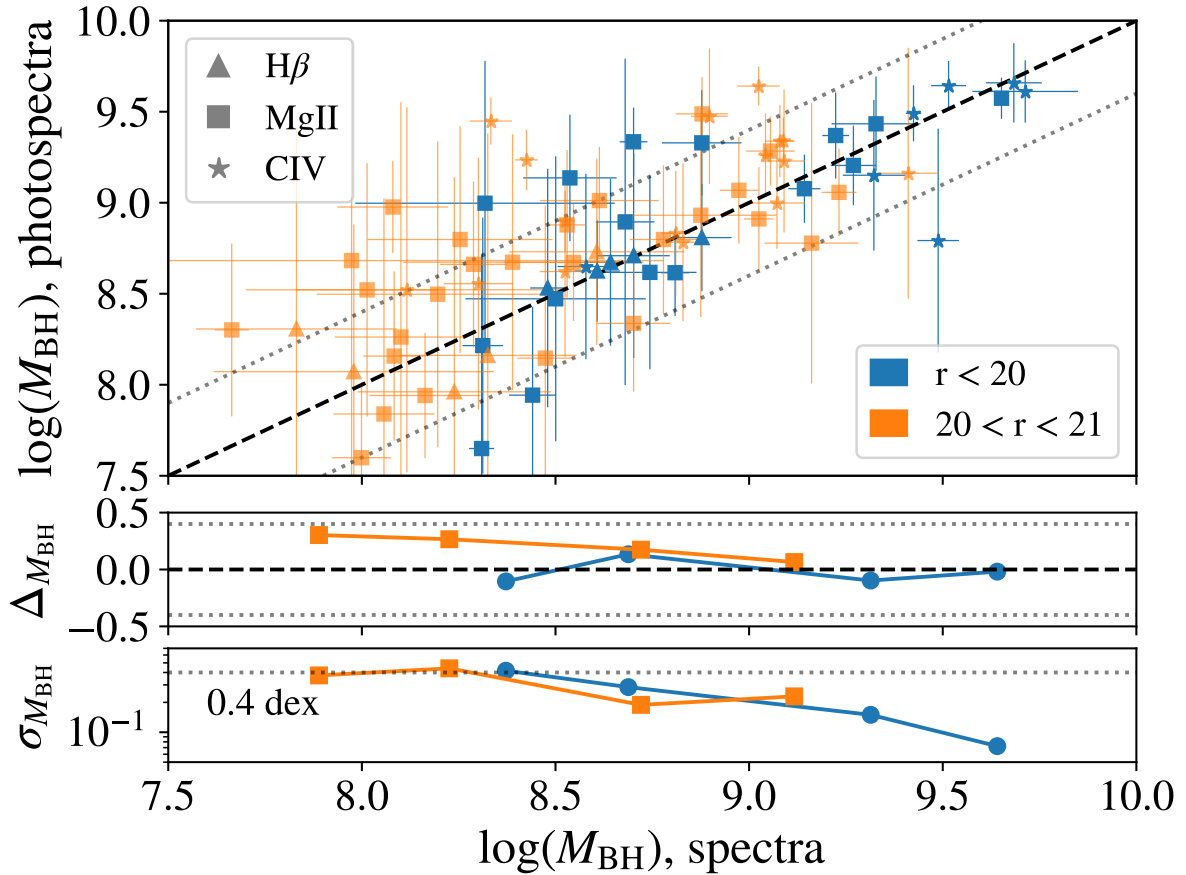


Figure 7. SMBH mass measurements from SDSS spectra and miniJPAS photospectra. The middle and bottom subpanels display the mean and standard deviation of the logarithmic difference between spectroscopic and photometric measurements, respectively, the dashed line indicates a 1:1 relation between these measurements, and dotted lines are displaced 0.4 dex from such relation. As we can see, there is a remarkable agreement between single-epoch spectroscopy and photometry masses, with most measurements less than 1σ away from the 1:1 relation.

from miniJPAS, finding that both are compatible within error bars. We also show that the standard deviation of the difference between spectroscopic and photometric measurements ranges from 0.4 to 0.07 dex for masses from $\log(M_{\text{BH}}/M_{\odot}) \approx 8$ to 9.75, respectively. Reverberation mapping studies show that SES masses are affected by systematic uncertainties of the order of 0.4 dex; given that single-epoch spectroscopy and photometry face similar systematics, we can conclude that single-epoch photometry yields SMBH virial masses with only mildly worse precision than single-epoch spectroscopy for the majority of sources in the validation sample.

Throughout this work, we focused on characterising the precision single-epoch photometry for the J-PAS survey, which will soon start observing thousands of square degrees of the northern sky without applying any source preselection other than the photometric depth in the detection band. Therefore, single-epoch photometry has the potential to provide details on the physical properties of new types of quasar populations not satisfying the preselection criteria of previous spectroscopic surveys. We have shown that our current technique delivers precise measurements only for sources brighter than $r = 21$; to push our technique towards fainter magnitudes, we plan to measure SMBH virial masses from stacked photospectra of low signal-to-noise sources. Taken together, we expect J-PAS and single-epoch photometry to be of paramount importance to complete our knowledge of SMBH demographics across cosmic time.

Finally, although our technique has been developed to anal-

yse J-PAS photospectra, single-epoch photometry can also be used to compute SMBH masses for quasars observed by other surveys without substantial modifications. For instance, we could use this methodology to analyse data from multi-band surveys with enough spectral resolution to resolve the profile of broad emission lines such as SHARDS and PAUS, and low-resolution spectroscopic surveys covering an extensive wavelength range like *Gaia* (Gaia Collaboration et al. 2012) and the Spectro-Photometer for the History of the Universe, Epoch of Reionization and Ices Explorer survey (SPHEREx; Doré et al. 2014).

ACKNOWLEDGEMENTS

This paper has gone through the internal review process of the J-PAS collaboration. We acknowledge useful discussion with Giorgio Calderone, Roberto Cid Fernandes and Rain Kipper and the feedback of Jifeng Liu. This work uses observations made with the JST/T250 telescope and PathFinder camera for the miniJPAS project at the Observatorio Astrofísico de Javalambre (OAJ) in Teruel, which is owned, managed, and operated by the Centro de Estudios de Física del Cosmos de Aragón (CEFCA). We acknowledge the OAJ Data Processing and Archiving Unit (UPAD) for reducing and calibrating miniJPAS data and the use of the Atlas EDR cluster at the Donostia International Physics Center (DIPC).

Funding for the J-PAS Project has been provided by the Governments of Spain and Aragón through the Fondo de Inversión de Teruel, European FEDER funding and the Spanish Ministry of Science, Innovation and Universities, and by the Brazilian agencies FINEP, FAPESP, FAPERJ and by the National Observatory of Brazil. Additional funding was also provided by the Tartu Observatory and by the J-PAS Chinese Astronomical Consortium. Funding for OAJ, UPAD, and CEFCA has been provided by the Governments of Spain and Aragón through the Fondo de Inversiones de Teruel; the Aragón Government through the Research Groups E96, E103, and E16_17R; the Spanish Ministry of Science, Innovation and Universities (MCIU/AEI/FEDER, UE) with grant PGC2018-097585-B-C21; the Spanish Ministry of Economy and Competitiveness (MINECO/FEDER, UE) under AYA2015-66211-C2-1-P, AYA2015-66211-C2-2, AYA2012-30789, and ICTS-2009-14; and European FEDER funding (FCDD10-4E-867, FCDD13-4E-2685). J.C.M. and S.B. acknowledge partial support from the grant PGC2018-097585-B-C22. B.T. acknowledges support from the Israel Science Foundation (grant number 1849/19). C.Q. acknowledges support from Brazilian funding agencies FAPESP and CAPES. L.A.D.G. and R.G.D. acknowledge financial support from the State Agency for Research of the Spanish MCIU through the “Center of Excellence Severo Ochoa” award to the Instituto de Astrofísica de Andalucía (SEV-2017-0709), and R.G.D. also does it to the projects AYA2016-77846-P and PID2019-109067-GB100. C.H.M. acknowledges financial support from the Spanish Ministry of Science, Innovation, and Universities through the project PGC2018-097585-B-C2.

DATA AVAILABILITY

In Table 1, we gather single-epoch photometry measurements for the quasar validation sample. An extended version of this table including single-epoch spectroscopy results can be found in [here](#).

SOFTWARE

This work made use of the following python packages: *ASTROPY* (Astropy Collaboration et al. 2013, 2018), *EMCEE* (Foreman-Mackey et al. 2013), *IPYTHON* (Perez & Granger 2007), *MATPLOTLIB* (Hunter 2007), *MPI4PY* (Dalcín et al. 2005, 2008; Dalcín et al. 2011; Dalcín & Fang 2021), *NUMPY* (Harris et al. 2020), *PYDOE2* (Rickard Sjögren and Daniel Svensson 2018), and *SCIPY* (Virtanen et al. 2020).

REFERENCES

- Abramo L. R., et al., 2012, *MNRAS*, **423**, 3251
- Abramowicz M. A., Fragile P. C., 2013, *Living Reviews in Relativity*, **16**, 1
- Aird J., et al., 2010, *Monthly Notices of the Royal Astronomical Society*, **401**, 2531
- Alarcon A., et al., 2021, *Monthly Notices of the Royal Astronomical Society*, **501**, 6103
- Astropy Collaboration et al., 2013, *Astronomy and Astrophysics*, **558**, A33
- Astropy Collaboration et al., 2018, *The Astronomical Journal*, **156**, 123
- Baldwin J. A., 1977, *The Astrophysical Journal*, **214**, 679
- Bañados E., et al., 2018, *Nature*, **553**, 473
- Benítez N., et al., 2009, *ApJ*, **691**, 241
- Benítez N., et al., 2014, arXiv e-prints, [p. arxiv:1403.5237](#)
- Bentz M. C., Peterson B. M., Pogge R. W., Vestergaard M., Onken C. A., 2006, *The Astrophysical Journal*, **644**, 133
- Bentz M. C., Peterson B. M., Netzer H., Pogge R. W., Vestergaard M., 2009, *The Astrophysical Journal*, **697**, 160
- Bentz M. C., et al., 2013, *The Astrophysical Journal*, **767**, 149
- Blandford R. D., McKee C. F., 1982, *The Astrophysical Journal*, **255**, 419
- Bonoli S., et al., 2021a, in Pović M., Marziani P., Masegosa J., Netzer H., Negu S. H., Tessema S. B., eds, *IAU Symposium Vol. 356, Nuclear Activity in Galaxies Across Cosmic Time*. pp 12–16, [doi:10.1017/S1743921320002483](#)
- Bonoli S., et al., 2021b, *Astronomy and Astrophysics*, **653**, A31
- Bontà E. D., et al., 2020, *The Astrophysical Journal*, **903**, 112
- Brauneck U., Sprengard R., Bourquin S., Marín-Franch A., 2018a, *Journal of Astronomical Telescopes, Instruments, and Systems*, **4**, 015002
- Brauneck U., Sprengard R., Bourquin S., Marín-Franch A., 2018b, *Journal of Astronomical Telescopes, Instruments, and Systems*, **4**, 015003
- Broyden C. G., 1970, *IMA Journal of Applied Mathematics*, **6**, 76
- Busca N. G., et al., 2013, *Astronomy and Astrophysics*, **552**, A96
- Calderone G., Nicastro L., Ghisellini G., Dotti M., Sbarrato T., Shankar F., Colpi M., 2017, *MNRAS*, **472**, 4051
- Caplar N., Lilly S. J., Trakhtenbrot B., 2017, *The Astrophysical Journal*, **834**, 111
- Castorina E., et al., 2019, *Journal of Cosmology and Astroparticle Physics*, **2019**, 010
- Chambers K. C., et al., 2016, The Pan-STARRS1 Surveys, <https://ui.adsabs.harvard.edu/abs/2016arXiv161205560C>
- Chaves-Montero J., et al., 2017, *Monthly Notices of the Royal Astronomical Society*, **472**, 2085
- Collin S., Kawaguchi T., Peterson B. M., Vestergaard M., 2006, *Astronomy and Astrophysics*, **456**, 75
- Cristiani S., Vio R., 1990, *Astronomy and Astrophysics*, **227**, 385
- Croton D. J., et al., 2006, *Monthly Notices of the Royal Astronomical Society*, **365**, 11
- Czerny B., Hryniewicz K., 2011, *Astronomy and Astrophysics*, **525**, L8
- Dalcín L., Fang Y.-L. L., 2021, *Computing in Science and Engineering*, **23**, 47
- Dalcín L., Paz R., Storti M., 2005, *Journal of Parallel and Distributed Computing*, **65**, 1108
- Dalcín L., Paz R., Storti M., D’Elía J., 2008, *Journal of Parallel and Distributed Computing*, **68**, 655
- Dalcín L. D., Paz R. R., Kler P. A., Cosimo A., 2011, *Advances in Water Resources*, **34**, 1124
- Davidson K., Netzer H., 1979, *Reviews of Modern Physics*, **51**, 715
- Davies R. I., et al., 2006, *The Astrophysical Journal*, **646**, 754
- Davies F. B., et al., 2018, *The Astrophysical Journal*, **864**, 142
- Davis M., et al., 2007, *ApJ*, **660**, L1
- Dawson K. S., et al., 2013, *The Astronomical Journal*, **145**, 10
- Dawson K. S., et al., 2016, *AJ*, **151**, 44
- Delvecchio I., et al., 2014, *Monthly Notices of the Royal Astronomical Society*, **439**, 2736
- Denney K. D., et al., 2016, *The Astrophysical Journal Supplement Series*, **224**, 14
- Di Matteo T., Springel V., Hernquist L., 2005, *Nature*, **433**, 604
- Dong X.-B., Wang T.-G., Wang J.-G., Fan X., Wang H., Zhou H., Yuan W., 2009, *The Astrophysical Journal*, **703**, L1
- Doré O., et al., 2014, arXiv e-prints, [p. arxiv:1412.4872](#)
- Dubois Y., Devriendt J., Slyz A., Teyssier R., 2012, *Monthly Notices of the Royal Astronomical Society*, **420**, 2662
- Eisenstein D. J., et al., 2011, *AJ*, **142**, 72
- Eriksen M., et al., 2019, *Monthly Notices of the Royal Astronomical Society*, **484**, 4200
- Fan X., et al., 2006, *AJ*, **132**, 117
- Ferrarese L., Merritt D., 2000, *The Astrophysical Journal*, **539**, L9
- Fletcher R., 1970, *The Computer Journal*, **13**, 317
- Foreman-Mackey D., Hogg D. W., Lang D., Goodman J., 2013, *PASP*, **125**, 306
- Gaia Collaboration et al., 2012, *Monthly Notices of the Royal Astronomical Society*, **423**, 3251
- Gebhardt K., et al., 2000, *ApJ*, **539**, L13
- Goldfarb D., 1970, *Mathematics of Computation*, **24**, 23

- González Delgado R. M., et al., 2021, *Astronomy and Astrophysics*, 649, A79
- Grandi S. A., 1982, *The Astrophysical Journal*, 255, 25
- Greene J. E., Ho L. C., 2005, *The Astrophysical Journal*, 630, 122
- Grier C. J., et al., 2019, *The Astrophysical Journal*, 887, 38
- Gültekin K., et al., 2009, *The Astrophysical Journal*, 698, 198
- Guo H., Shen Y., Wang S., 2018, *Astrophysics Source Code Library*, p. ascl:1809.008
- Guo H., Liu X., Shen Y., Loeb A., Monroe T., Prochaska J. X., 2019, *Monthly Notices of the Royal Astronomical Society*, 482, 3288
- Harris C. R., et al., 2020, *Nature*, 585, 357
- Hernán-Caballero A., Hatziminaoglou E., Alonso-Herrero A., Mateos S., 2016, *Monthly Notices of the Royal Astronomical Society*, 463, 2064
- Hernán-Caballero A., et al., 2021, arXiv e-prints, p. arXiv:2108.03271
- Hicks E. K. S., Malkan M. A., 2008, *The Astrophysical Journal Supplement Series*, 174, 31
- Ho L., 1999, Supermassive Black Holes in Galactic Nuclei: Observational Evidence and Astrophysical Consequences, doi:10.1007/978-94-011-4750-7_11
- Homayouni Y., et al., 2020, *The Astrophysical Journal*, 901, 55
- Hook I. M., McMahon R. G., Boyle B. J., Irwin M. J., 1994, *Monthly Notices of the Royal Astronomical Society*, 268, 305
- Hopkins P. F., et al., 2004, *The Astronomical Journal*, 128, 1112
- Hou J., et al., 2021, *Monthly Notices of the Royal Astronomical Society*, 500, 1201
- Hoyle F., Fowler W. A., 1963, *Monthly Notices of the Royal Astronomical Society*, 125, 169
- Hunter J. D., 2007, *Computing in Science and Engineering*, 9, 90
- Inayoshi K., Visbal E., Haiman Z., 2020, *Annual Review of Astronomy and Astrophysics*, vol. 58, p.27-97, 58, 27
- Jensen T. W., et al., 2016, *ApJ*, 833, 199
- Kaspi S., Smith P. S., Netzer H., Maoz D., Jannuzi B. T., Giveon U., 2000, *The Astrophysical Journal*, 533, 631
- Kaspi S., Maoz D., Netzer H., Peterson B. M., Vestergaard M., Jannuzi B. T., 2005, *The Astrophysical Journal*, 629, 61
- Kaspi S., Brandt W. N., Maoz D., Netzer H., Schneider D. P., Shemmer O., Grier C. J., 2021, arXiv e-prints, 2106, arXiv:2106.00691
- Kelly B. C., Bechtold J., Siemiginowska A., 2009, *The Astrophysical Journal*, 698, 895
- King A., 2003, *The Astrophysical Journal*, 596, L27
- Kollatschny W., Zetzl M., 2013, *Astronomy and Astrophysics*, 549, A100
- Kormendy J., Ho L. C., 2013, *Annual Review of Astronomy and Astrophysics*, 51, 511
- Kormendy J., Richstone D., 1995, *ARA&A*, 33, 581
- Kozłowski S., Kochanek C. S., Ashby M. L. N., Assef R. J., Brodwin M., Eisenhardt P. R., Jannuzi B. T., Stern D., 2016, *The Astrophysical Journal*, 817, 119
- Lira P., et al., 2018, *The Astrophysical Journal*, 865, 56
- Lumbreras-Calle A., et al., 2019, *Astronomy and Astrophysics*, 621, A52
- Lynden-Bell D., 1969, *Nature*, 223, 690
- MacLeod C. L., et al., 2010, *The Astrophysical Journal*, 721, 1014
- MacLeod C. L., et al., 2012, *The Astrophysical Journal*, 753, 106
- Magorrian J., et al., 1998, *The Astronomical Journal*, 115, 2285
- Marinello M., et al., 2020, *Monthly Notices of the Royal Astronomical Society*, 492, 1991
- Martínez-Solauche G., et al., 2021, *Astronomy and Astrophysics*, 647, A158
- McConnell N. J., Ma C.-P., 2013, *The Astrophysical Journal*, 764, 184
- McKay M. D., Beckman R. J., Conover W. J., 1979, *Technometrics*, 21, 239
- McLure R. J., Jarvis M. J., 2002, *Monthly Notices of the Royal Astronomical Society*, 337, 109
- Mejía-Restrepo J. E., Lira P., Netzer H., Trakhtenbrot B., Capellupo D. M., 2018, *Nature Astronomy*, 2, 63
- Merloni A., Rudnick G., Di Matteo T., 2004, *Monthly Notices of the Royal Astronomical Society*, 354, L37
- Meusinger H., Weiss V., 2013, *Astronomy and Astrophysics*, 560, A104
- Moles M., et al., 2008, *AJ*, 136, 1325
- Nagao T., Marconi A., Maiolino R., 2006, *Astronomy and Astrophysics*, 447, 157
- Netzer H., Peterson B. M., 1997, *Astronomical Time Series*, 218, 85
- Oke J. B., Gunn J. E., 1983, *The Astrophysical Journal*, 266, 713
- Oke J. B., Shields G. A., Korycansky D. G., 1984, *The Astrophysical Journal*, 277, 64
- Onken C. A., et al., 2007, *The Astrophysical Journal*, 670, 105
- Palanque-Delabrouille N., et al., 2013, *Astronomy and Astrophysics*, 551, A29
- Palanque-Delabrouille N., et al., 2016, *Astronomy and Astrophysics*, 587, A41
- Pâris I., et al., 2017, *A&A*, 597, A79
- Pâris I., et al., 2018, *Astronomy & Astrophysics*, 613, A51
- Perez F., Granger B. E., 2007, *Computing in Science Engineering*, 9, 21
- Pérez-González P. G., et al., 2013, *The Astrophysical Journal*, 762, 46
- Peterson B. M., 1993, *Publications of the Astronomical Society of the Pacific*, 105, 247
- Peterson B. M., 2014, *Space Science Reviews*, 183, 253
- Pieri M. M., et al., 2016, in Reylé C., Richard J., Cambréys L., Deleuil M., Pécontal E., Tresse L., Vauglin I., eds, SF2A-2016: Proceedings of the Annual meeting of the French Society of Astronomy and Astrophysics. pp 259–266 (arXiv:1611.09388)
- Pillepich A., et al., 2018, *MNRAS*, 473, 4077
- Planck Collaboration et al., 2014, *A&A*, 571, A16
- Rakshit S., Stalin C. S., Kotilainen J., 2020, *The Astrophysical Journal Supplement Series*, 249, 17
- Richards G. T., et al., 2011, *The Astronomical Journal*, 141, 167
- Rickard Sjögren and Daniel Svensson 2018, pyDOE2: An Experimental Design Package for Python, clicumu, <https://github.com/clicumu/pyDOE2>
- Risaliti G., Lusso E., 2019, *Nature Astronomy*, 3, 272
- Salpeter E. E., 1964, *The Astrophysical Journal*, 140, 796
- Schaye J., et al., 2015, *MNRAS*, 446, 521
- Shankar F., Weinberg D. H., Miralda-Escudé J., 2009, *The Astrophysical Journal*, 690, 20
- Shanno D. F., Kettler P. C., 1970, *Mathematics of Computation*, 24, 657
- Shen Y., 2013, *Bulletin of the Astronomical Society of India*, 41, 61
- Shen Y., et al., 2011, *The Astrophysical Journal Supplement Series*, 194, 45
- Shen Y., et al., 2016, *The Astrophysical Journal*, 831, 7
- Shen Y., et al., 2019, *The Astrophysical Journal Supplement Series*, 241, 34
- Sijacki D., Vogelsberger M., Genel S., Springel V., Torrey P., Snyder G. F., Nelson D., Hernquist L., 2015, *Monthly Notices of the Royal Astronomical Society*, 452, 575
- Silk J., Rees M. J., 1998, *Astronomy and Astrophysics*, 331, L1
- Silverman J. D., et al., 2008, *The Astrophysical Journal*, 679, 118
- Sobral D., Santos S., Matthee J., Paulino-Afonso A., Ribeiro B., Calhau J., Khostovan A. A., 2018, *Monthly Notices of the Royal Astronomical Society*, 476, 4725
- Somerville R. S., Hopkins P. F., Cox T. J., Robertson B. E., Hernquist L., 2008, *Monthly Notices of the Royal Astronomical Society*, 391, 481
- Taniguchi Y., et al., 2015, *Publications of the Astronomical Society of Japan*, 67, 104
- Tokunaga A. T., Vacca W. D., 2005, *Publications of the Astronomical Society of the Pacific*, 117, 421
- Trakhtenbrot B., Netzer H., 2012, *Monthly Notices of the Royal Astronomical Society*, 427, 3081
- Vanden Berk D. E., et al., 2001, *AJ*, 122, 549
- Véron-Cetty M.-P., Joly M., Véron P., 2004, *Astronomy & Astrophysics*, 417, 515
- Vestergaard M., 2002, *The Astrophysical Journal*, 571, 733
- Vestergaard M., Peterson B. M., 2006, *The Astrophysical Journal*, 641, 689
- Virtanen P., et al., 2020, *Nature Methods*, 17, 261
- Wandel A., Peterson B. M., Malkan M. A., 1999, *The Astrophysical Journal*, 526, 579
- Wang J.-M., et al., 2014, *ApJ*, 793, 108
- Wang F., et al., 2020, *The Astrophysical Journal*, 896, 23
- Wang F., et al., 2021, arXiv e-prints, p. arXiv:2101.03179
- Watson D., Denney K. D., Vestergaard M., Davis T. M., 2011, *ApJ*, 740, L49
- Weinberger R., et al., 2017, *MNRAS*, 465, 3291

- Williams P. R., et al., 2018, *The Astrophysical Journal*, 866, 75
 Wills B. J., Netzer H., Wills D., 1985, *The Astrophysical Journal*, 288, 94
 Yang G., et al., 2018, *Monthly Notices of the Royal Astronomical Society*, 475, 1887
 Yang J., et al., 2020a, *The Astrophysical Journal*, 897, L14
 Yang J., et al., 2020b, *The Astrophysical Journal*, 904, 26
 York D. G., et al., 2000, *AJ*, 120, 1579
 van Dokkum P. G., et al., 2009, *Publications of the Astronomical Society of the Pacific*, 121, 2

AFFILIATIONS

- ¹ Donostia International Physics Center, Paseo Manuel de Lardizabal 4, E-20018 Donostia-San Sebastian, Spain.
² Ikerbasque, Basque Foundation for Science, E-48013 Bilbao, Spain.
³ School of Physics and Astronomy, Tel Aviv University, Tel Aviv 69978, Israel.
⁴ Facultad de Ciencias Físicas, Universidad Complutense de Madrid, Plaza de Ciencias, 1, 28040 Madrid, Spain.
⁵ Departamento de Astronomia, Instituto de Física, Universidade Federal do Rio Grande do Sul (UFRGS), Av. Bento Gonçalves 9500, Porto Alegre, RS, Brazil.
⁶ Instituto de Física, Universidade de São Paulo, Rua do Matão 1371, CEP 05508-090, São Paulo, Brazil.
⁷ Instituto de Astrofísica de Andalucía (CSIC), P.O. Box 3004, 18080 Granada, Spain.
⁸ Centro de Estudios de Física del Cosmos de Aragón (CEFCA), Plaza San Juan, 1, E-44001 Teruel, Spain.
⁹ Instituto de Astrofísica de Canarias, Calle Vía Láctea SN, ES38205 La Laguna, Spain.
¹⁰ Departamento de Astrofísica, Universidad de La Laguna, ES38205 La Laguna, Spain.
¹¹ Centro de Estudios de Física del Cosmos de Aragón (CEFCA), Unidad Asociada al CSIC, Plaza San Juan, 1, E-44001 Teruel, Spain.
¹² Observatório Nacional/MCTIC, Rua General José Cristino, 77, São Cristóvão, Rio de Janeiro, RJ 20921-400, Brazil.
¹³ Institute of Astronomy, Geophysics and Atmospheric Sciences, University of São Paulo, Rua do Matão, 1226, São Paulo, SP 05508-090, Brazil.
¹⁴ Department of Physics, Lancaster University, Lancaster, LA1 4YB, UK.
¹⁵ Instituto de Física, Universidade Federal da Bahia, 40210-340, Salvador, BA, Brazil.
¹⁶ Department of Astronomy, University of Michigan, 311 West Hall, 1085 South University Ave., Ann Arbor, USA.
¹⁷ University of Alabama, Department of Physics and Astronomy, Gallalee Hall, Tuscaloosa, AL 35401, USA.
¹⁸ Instruments4, 4121 Pembury Place, La Canada Flintridge, CA 91011, USA.

APPENDIX A: FORWARD- VS BACKWARD-MODELLING OBSERVATIONS

In this section, we study if we can extract unbiased measurements of emission line widths by backward-modelling quasar observations.

To backward-modelling emission line widths, we first estimate the quasar continuum emission following the same approach as in §3.2, and then we subtract it from observations to produce a line-only spectrum. After that, we identify the J–PAS bands in which the

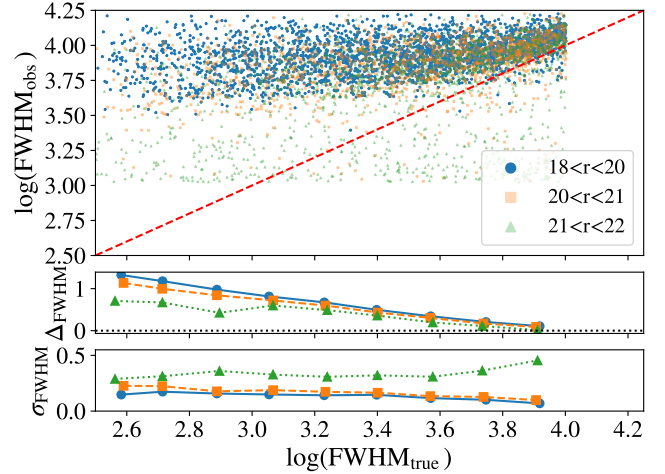


Figure A1. Backward-modelling measurements of C iv FWHM from simulated J–PAS observations. This approach results in biased FWHM measurements even for lines as wide as $10\,000\text{ km s}^{-1}$, while forward-modelling observations enables FWHM of lines broader than 1500 km s^{-1} in an unbiased fashion.

centre of the broad emission lines H β , Mg II, and C iv fall; if one of these lines falls between two J–PAS bands, we select the band with the maximum flux. Finally, we compute the FWHM of each line by subtracting the wavelengths at which the continuum emission intercepts half the flux of the band at which the centre of the line falls. Note that we perform a linear interpolation of the flux between J–PAS bands to improve the resolution of the results.

In §3.5, we use simulated J–PAS photospectra to study the impact of both the limited spectral resolution of J–PAS and photometric errors on single-epoch photometry. In Fig. A1, we show the result of backward-modelling the C iv width from simulated J–PAS observations. We can readily see that this approach results in biased FWHM measurements even for emission lines as broad as $10\,000\text{ km s}^{-1}$. In Fig. 3, we show that forward-modelling observations enables measuring the FWHM of lines as narrow as 1500 km s^{-1} in an unbiased fashion, thereby pushing the accuracy of the results by almost an order of magnitude relative to backward-modelling. We thus conclude that forward-modelling observations is crucial for unbiased estimation of emission line properties from narrow-band surveys.

APPENDIX B: IMPACT OF PHOTOMETRIC REDSHIFT ERRORS

In §4, we use spectroscopic redshift estimates to conduct single-epoch photometry measurements. The J–PAS survey will soon observe hundreds of thousands of quasars for which we will only have access to photometric redshift estimates. In this section, we study the impact of photometric redshift errors on single-epoch photometry measurements.

Forecasts for the J–PAS survey and preliminary results from the miniJPAS survey suggest that the precision of photometric redshifts for J–PAS quasars will be $\approx 0.5\%$ (Abramo et al. 2012; Chaves-Montero et al. 2017; Bonoli et al. 2021b). To study the impact of this level of uncertainties on single-epoch photometry results, we first perturb the actual redshift of simulated J–PAS observations (see §3.5) according to a Gaussian of width $\sigma_z = 0.005(1+z)$, and then we apply our methodology. In Fig. B1, we show the precision of

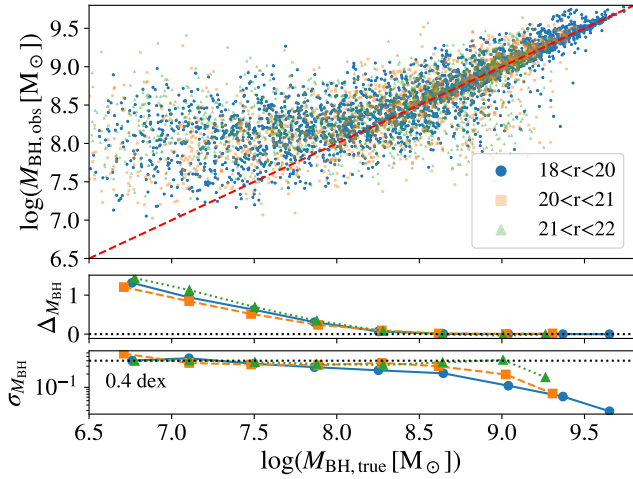


Figure B1. Dependence of single-epoch photometry masses upon the level of photometric redshift errors expected for J–PAS quasars. Using simulated J–PAS observations, we find that the impact of these errors on SEP masses is negligible.

SEP masses measured from this sample. By comparing the results shown in this figure and the lower-right panel of Fig. 3, we can readily see that the impact of photometric redshift errors on SEP masses is negligible for the level of errors expected for J–PAS.

It is important to note that the previous approach does not account for the possibility of redshift outliers, i.e. sources with photometric redshift estimate very far from their actual redshift primarily due to low SNR observations and line confusion (e.g., Chaves-Montero et al. 2017). We expect minimal impact of the first type of outliers because we only analyse sources brighter than $r = 21$. On the other hand, outliers caused by line confusion are more problematic because these can be brighter than $r = 21$, and our code will return precise measurements of the misclassified line. We will carry out a more detailed study about this source of uncertainty in future works.

This paper has been typeset from a \LaTeX file prepared by the author.